Title

Development and Implementation of a Vehicle-Centered Fault Diagnostic and Management System for the Extended PATH-AHS Architecture: Part II

Authors

Yi, Jingang
Suryanarayanan, Shashikanth
Howell, Adam
et al.

Publication Date

2002-11-01

CALIFORNIA PATH PROGRAM
INSTITUTE OF TRANSPORTATION STUDIES
UNIVERSITY OF CALIFORNIA, BERKELEY

Development and Implementation of a Vehicle-Centered Fault Diagnostic and Management System for the Extended PATH-AHS Architecture: Part II

Jingang Yi, Shashikanth Suryanarayanan, Adam Howell, Roberto Horowitz, Masayoshi Tomizuka, Karl Hedrick
University of California, Berkeley

California PATH Research Report
UCB-ITS-PRR-2002-35

This work was performed as part of the California PATH Program of the University of California, in cooperation with the State of California Business, Transportation, and Housing Agency, Department of Transportation; and the United States Department of Transportation, Federal Highway Administration.

Final Report for Task Order 4207

November 2002

ISSN 1055-1425

Development and Implementation of a Vehicle-Centered Fault Diagnostic and Management System for the Extended PATH-AHS Architecture: Part II

Jingang Yi, Shashikanth Suryanarayanan, Adam Howell,
Roberto Horowitz, Masayoshi Tomizuka, Karl Hedrick

Department of Mechanical Engineering
University of California at Berkeley

August 6, 2002

ABSTRACT

This project is a continuation of MOU 373. It concludes ongoing research to extend and integrate existing results on fault diagnostic and fault management research, and develop a comprehensive fault management system. Features include a multi-layer fault diagnostic and management system, diagnosis of faults in the sensors and actuators of the lateral and longitudinal control systems, detection of faults in the most vital sensors and actuators, and development of a systematic methodology for processing diagnostic residues. Experimental implementation and testing of the completed system is carried out in this project. This work is important because fault diagnostics and management appear to be the most important technical issues remaining to be resolved before vehicle automation can be implemented. "Soft" faults such as tire/road conditions variations have been extended in this project. An analytical model for calculating the longitudinal and lateral traction/braking forces and the self-alignment moment and the effect of wet road conditions on the tire/road friction model have been discussed and developed in this project.

KEYWORDS

Fault diagnostics, fault handling, automated highway systems (AHS), fault observers/filters, LuGre friction model, tire/road friction estimation

ACKNOWLEDGMENT

This work was executed under grant Task Order 4207 of the the Institute of Transportation Studies at the University of California at Berkeley and part of a large effort to develop the experimental development. The authors would specially like to thank support staffs at RFS at UC Berkeley in USA and Dr. Xavier Claeys at Renault Inc. in France for all of their help, suggestions and comments.

Executive Summary

This project is a continuation of MOU 373. It concludes ongoing research to extend and integrate existing results on fault diagnostic and fault management research, and develop a comprehensive fault management system. Features include a multi-layer fault diagnostic and management system, diagnosis of faults in the sensors and actuators of the lateral and longitudinal control systems, detection of faults in the most vital sensors and actuators, and development of a systematic methodology for processing diagnostic residues. The bulk of the research presented in this report was done as part of PATH-Caltrans Task Order 4207.

The research documented in this report primarily focuses on experimental verification of fault management in the regulation layer of the PATH AHS architecture and an extension of the "soft" faults diagnostics and handling. The regulation layer consists of the lateral and longitudinal control laws that interact directly with the sensors and actuators on-board the PATH vehicles.

Since the lateral and longitudinal dynamics of the vehicles are vastly different in their behavior, different approaches have been adopted for fault management systems of each of these subsystems. In the project MOU 373 (Yi et al., 2002), fault tolerance in the lateral control subsystem is realized mainly through the use of fault tolerant lateral control laws whereas a "classical" approach for fault tolerant control design was used for the longitudinal control system. "Soft" faults detection and handling, particularly the tire/road interactions and emergency braking maneuvers, have also been investigated in MOU 373.

One of the major contributions of this research is the successful implementation and test of a comprehensive failure management system for the regulation layer of the PATH AHS architecture on real vehicle testing facilities in RFS at UC Berkeley campus. Fault tolerant lateral control laws, failure detection filters for the lateral and longitudinal control subsystems have been implemented and tested both at low and high speeds on the Buick LeSabre vehicles at PATH. The experimental results verify the design and development in MOU 373. The design methodologies and results of this effort in conjunction with the results of MOU 384/TO 4204 (Vehicle Lateral Control under Fault in the Front/Rear Sensors) are aimed for use in the development of fault tolerant lateral and longitudinal control systems (TO 4205, TO 4206) for heavy vehicles to be used in Demo 2003.

Another major contribution of this research is the extension of a dynamic tire/road friction model under various conditions, which is an important part of "soft" faults diagnostics and handling. Effects of different physical conditions on the tire/road friction characteristics have been analyzed. Particularly, two case studies were investigated. We first derived a three dimensional dynamic tire/road friction model, based on previous work which had only considered longitudinal motions. Both distributed and lumped friction models were discussed. The lumped model can be used to identify the tire/road conditions and can be applied to vehicle control. A numerical example was presented to calibrate the model parameters and validate the model with respect to the widely used "magic for-

mula". From the analysis and numerical results obtained, we found that the derived friction model can capture the tire/road friction characteristics and can easily be used for friction estimation and control purposes. Secondly, we discussed both the hydro-dynamic and lubrication effects of the contact zone on friction models under wet road conditions. Different road textures and densities were introduced in the LuGre friction tire models using relatively simple methods. Furthermore, a technique to decouple the effects of the road pavement from those of the tire under wet conditions was proposed and some numerical examples, which illustrated the theoretical developments, were included.

Contents

List of Figures

List of Tables

Chapter 1

Introduction

1.1 Background

Over the last ten years, PATH's Advanced Vehicle Control System effort has made impressive strides in the modeling, control design and implementation of several vehicle control laws. Since the 1997 NAHSC [1] demonstration on the I-15 lanes in San Diego, PATH's research focus has shifted towards deployment related issues encountered in Automated Highway Systems (AHS) development such as safety and reliability.

To satisfy requirements of safety, the AHS should be designed such that the automated vehicles function safely under nominal operating conditions as well as under "abnormal"or faulty conditions that arise during highway operation. The nominal operating environment assumes the faultless operation of the system components and benign environmental conditions. The abnormal operating conditions are caused by faults.

Several prior and on-going research efforts (Demo 97 preparations, MOU 384, MOUs 288/312, etc.) at PATH have dedicated a great deal of effort towards the design of a robust controllers for both modes of operation. Normal mode control laws at the regulation, coordination and link layer have been developed and tested in simulations and experiments. Fault detection algorithms for the on-board sensor and actuator critical to automated control have been developed and tested in simulations and experiments (Garg, 1995; Chung et al., 1996; Chung et al., 1997; Patwardhan, 1994; Agogino et al., 1997; Rajamani et al., 1997; Rajamani et al., 2001; Yi et al., 2001). At the same time, fault handling schemes using new maneuvers and control laws have been designed for degraded modes of operation to ensure that the safety of the AHS is maintained and the performance loss is minimized in abnormal situations (Lygeros et al., 2000; Godbole et al., 2000; Chen et al., 1997; Yi et al., 2001). In addition, these fault handling schemes have been successfully tested in the SmartPATH and SmartAHS simulation program (Carbaugh et al., 1997; Yi et al., 2001).

This project is a continuation of MOU 373. The goal of this project is to extend and improve these developments in the areas of fault diagnostics and fault handling with the existing control hierarchy (Varaiya, 1993) to produce a complete fault tolerant AHS control system that can be implemented on the vehicles and the roadway. The project concentrates on the design of a fault tolerant AHS control system that can detect and handle both hard and soft faults in the lateral and longitudinal control systems. However, acts of nature, such as earthquakes, floods, etc. and obstacles on the

[1] National Highway System Consortium.

road are not considered in order to limit the scope of the project. In other words, the project intends to develop and implement subsystems that fit into the the overall structure of a fault tolerant AHS control system as shown schematically in Fig. 1.1. The project primarily focuses on development related to the regulation layer namely the lateral and longitudinal control subsystems.

The research documented in this report primarily focuses on experimental verification of fault management in the regulation layer of the PATH AHS architecture and an extension of the "soft" faults diagnostics and handling. The regulation layer consists of the lateral and longitudinal control laws that interact directly with the sensors and actuators on-board the PATH vehicles.

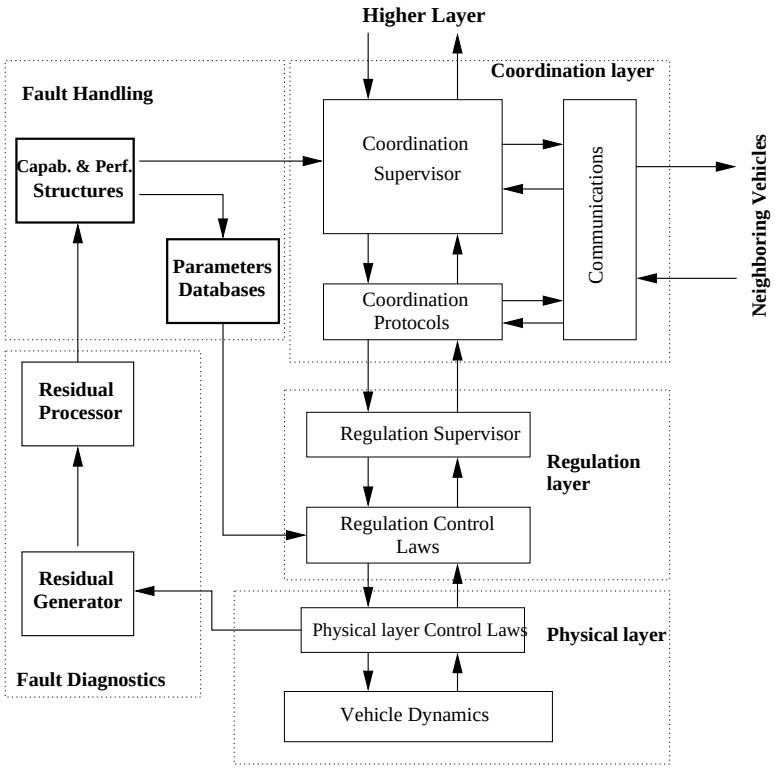

Figure 1.1: Extended hierarchical fault tolerant AHS controller

Fig. 1.2 depicts the fault tolerant system design framework discussed in MOU 373 (Yi et al., 2002). The fault tolerant design framework attempts to incorporate fault tolerance **apriori** into system design. The framework is based on the argument that important design decisions (such as those shown in Fig. 1.2) made during the design process of an automated system have a direct bearing on the fault tolerance of the resulting automated system. Therefore, each design decision needs to be judiciously made based on, amongst other considerations, the issue of fault tolerance of the resulting system.

We now mention where relevant past/present research activity at PATH fit in into this overall design framework.

- Demo 97: longitudinal and lateral control design, rudimentary failure detection and diagnosis issues associated with the radar
- MOU 289, MOU 313, MOU 385: Lateral control design for heavy vehicles

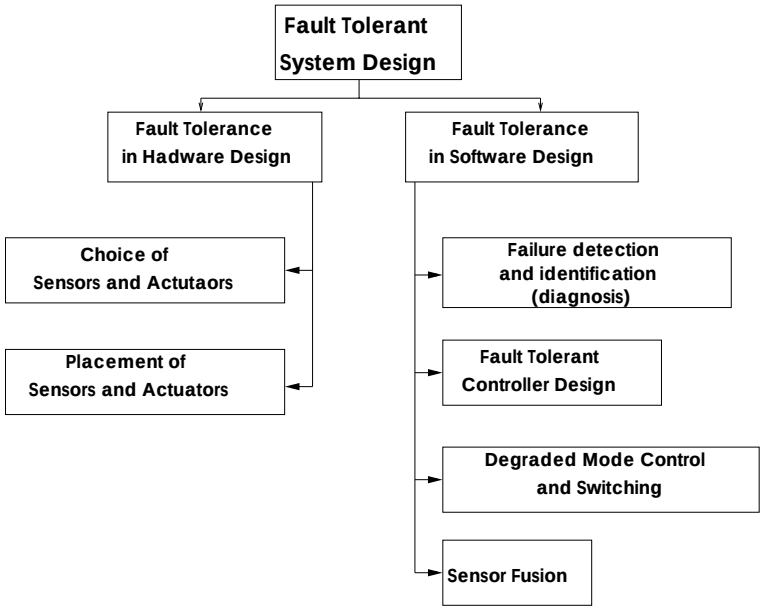

Figure 1.2: Fault Tolerant Design Framework

- MOU 292, MOU 314, MOU 372: Longitudinal control design for heavy vehicles
- MOU 312, **MOU 373, TO 4207**: failure detection and diagnosis systems for the longitudinal control system, fault tolerant control schemes for the lateral control system, soft fault handling: tire-road friction estimation and emergency braking control.
- MOU 384, TO 4204: Degraded mode control schemes for lane-keeping control under failure of the front/rear magnetometers
- TO 4205, TO 4206: sensor placement and integration of all prior research aimed at a fault tolerant design framework for lateral and longitudinal control subsystems to be implemented on buses

1.2 Organization of Report

This report primarily discusses the continuation work of MOU 373. It focuses on experimental verification of fault management in the regulation layer of the PATH AHS architecture and an extension of the "soft" faults diagnostics and handling.

Chapter 2 deals with the experimental verification of the fault tolerant vehicle control systems developed in MOU 373. In MOU 373, we demonstrated fault tolerant lateral vehicle controller design based on simultaneous stabilization and on the concept of observer based look-ahead. In this report, we present the experimental results for these control laws. For longitudinal fault tolerant vehicle control systems, in MOU 373 we only showed the system performance under no fault scenario and under faults in the physical layer control components. In this report, we will show the performance under faults in the regulation layer control components.

In Chapter 3, we discussed the formulation of a general physical tire/road friction model under various conditions. This is an important part of “soft” faults diagnostics and handling. Effects of different physical conditions on the tire/road friction characteristics are analyzed. Particularly, two case studies are investigated. We first derive a three dimensional dynamic tire/road friction model, based on previous work which had only considered longitudinal motions. Secondly, we discuss both the hydro-dynamic and lubrication effects of the contact zone on friction models under wet road conditions. Different road textures and densities are introduced in the LuGre friction tire models using relatively simple methods. Furthermore, a technique to decouple the effects of the road pavement from those of the tire under wet conditions is proposed and some numerical examples, which illustrate the theoretical developments, are included. Future research directions in this area are also presented in this chapter.

Chapter 2

Experimental Validation of Fault Tolerant Vehicle Control System

In MOU 373, both lateral and longitudinal fault tolerant vehicle control systems have been developed (Yi et al., 2002). For the lateral control system,a new approach to failure management (in its components) has been adopted. This deals with the design of fault tolerant controllers which are insensitive to certain faults that may occur during operation of the vehicles. For the longitudinal control system, a classical approach to fault tolerant control design was taken and fault tolerance of the controller is provided by the addition of the fault diagnostic system and fault management system. The fault diagnostic system monitors the condition of the vehicle via sensor measurement and command inputs, and communicates the current status to the fault management system. The fault management system uses this information, as well as the current mode of operation and other control objectives, to decide what corrective action should be taken when a fault has been declared. Simulation results have been used to validate the lateral fault tolerant control systems. Limited experimental testing has been conducted to verify the longitudinal system performance under faults in the physical layer control components.

In this Chapter, we will discuss the experimental validations for both lateral and longitudinal fault tolerant control systems. In section 2.1, we focus on lateral fault tolerant controller design based on both simultaneous stabilization and the concept of observer based look-ahead. In section 2.2, we concentrate on performance of longitudinal fault tolerant vehicle control systems under faults in regulation layer control components.

2.1 Experimental Testing of Fault Tolerant Lateral Control Algorithms

In this section we present results of experimental testing of the lateral fault tolerant controllers discussed in Chapter 3 in Yi et al. (2002). The experimental tests described in this section are:

1. Performance of simultaneous stabilization based fault tolerant controller (tolerant to fault #3):
   (a) Low speed test with rear magnetometer failure
   (b) High speed test with rear magnetometer failure

(c) Low speed test with front magnetometer failure

2. Observer based look-ahead scheme (tolerant to fault #2):

   (a) Low speed test with rear magnetometer failure

During the tests, the failure is emulated. For example to test control performance when fault #3 occurs, the magnetometer output is **manually** set to zero. The low speed and high speed tests were performed at Richmond Field Station and Crows Landing respectively.

2.1.1 Performance of simultaneous stabilization based fault tolerant controller

Figs. 2.1, 2.2 and 2.3 show experimental results for the simultaneous stabilization based faulty tolerant controller (tests described above).

We observe that under failure of the rear magnetometer (figures 2.1, 2.2) satisfactory control action can still be achieved. At high speeds, for a d_s value of 1.5m, good control action can be achieved on the Buick LeSabre up to about 55-60 mph. For speeds higher than this, oscillations start to creep in. Low speed performance under failure of the front magnetometer is far from satisfactory. This is because if the front magnetometer yields a zero output, the vehicle is practically under the control of the rear magnetometer. Suryanarayan and Tomizuka show in (Suryanarayanan and Tomizuka, 2001) that rear magnetometer based control of vehicles at low speeds is very difficult to achieve and for practical purposes impossible. Fault tolerance tests under failure of the front magnetometer at high speeds has not been tested completely as yet.

2.1.2 Performance of observer based look-ahead scheme based controller

Fig. 2.4 shows experimental results for the *observer based look-ahead* based fault tolerant controller (described in the beginning of this section).

In the interest of brevity, we do not include the performance of the observer based scheme when fault #3 occurs. Experimental results included below demonstrate success of the scheme under fault #2. High speed tests for the observer based look-ahead scheme is currently underway. Under failure of the front magnetometer, the observer based controller performs poorly (as expected) at low longitudinal velocities.

We observe that for the failure of the front magnetometer, the observer based controller has a performance very similar to the simultaneous stabilization based controller. However, it is was observed that the observer based controller is significantly more difficult to implement in practice since precise estimates of the vehicle states are required over wide ranges of longitudinal velocities.

2.2 Experimental Testing of Fault Tolerant Longitudinal Control Algorithms Under Faults in the Regulation Layer Control Components

The fault diagnostic system presented in the previous two sections was implemented in the C programming language as an addition to the longitudinal control software developed for the 1997

NAHSC Demonstration (Staff, 1998). This longitudinal control code has been extensively tested and used by PATH, and provided much of the underlying software structure needed by the diagnostic system, such as access to the publish-subscribe database and the command inputs calculated by the controller.

The fault diagnostic code was tested under two scenarios; low-speed real-time tests on a single car at Richmond Field Station (RFS) and emulation using data from both low and high-speed tests on a platoon of three vehicles on I-15 in San Diego. This section will focus on results using the data from I-15, since the single-vehicle tests at RFS were used primarily to debug and verify the timing latencies of the additional fault diagnostic software.

The experimental tests conducted on I-15 used a platoon of three Buick LeSabre, where the lead vehicle followed a desired velocity profile and the two following vehicles attempted to maintain a constant distance from the preceding vehicle. For the experimental data shown in this report, the cruise speed was set to 60 mph with a desired spacing of 12 meters. To simplify the testing procedure, no additional maneuvers were performed during any of the tests.

To eliminate the need for hardware modifications, the occurrence of faults in the control components were simulated in the longitudinal control software during the experimental runs. For example, sensor faults were simulated by adding a time-varying bias to the sensor reading before the control calculations were performed. Similarly, actuator faults were simulated by adding a time-varying bias to the actuator command after the control calculations were performed. The remainder of this section will demonstrate the performance of the implemented diagnostic system under both normal and faulty conditions.

Figs. 2.5 through 2.12 show the experimental results for the same testing scenario as in Chapter 4 in Yi et al. (2002) with the addition of a time-varying in each of the regulation layer control components. For each fault in both this section and the next, two sets of plots will demonstrate the main aspects of the residual processing involved for each specific fault. Plots of the residuals and observer estimates have been omitted for brevity. The sets of four plots depict the fault mode estimates for each of the components normalized by their thresholds, while the sets of two plots show the fault identified by the residual processor and it's estimated magnitude. Also on the second set of plots is an indication of when the engine is at idle to indicate when the residual processing is disabled for the physical layer control components.

Magnetometer and accelerometer faults can clearly be detected and identified as shown in Figs. 2.5 through 2.8. However, the faults in the accelerometer can only be detected if larger than about $0.6m/sec^2$ due to modeling uncertainty and the relative inaccuracy of the sensor. Faults in the wheel speed sensor are closely coupled to radar faults, making the identification very sensitive to the choice of thresholds as seen in Figs. 2.9 and 2.10. Finally, the radar faults are obviously not easily detectable as shown in Figs. 2.11 through 2.12. However, this lost sensitivity and close coupling between the wheel speed and radar faults is primarily due to the range observer used for the regulation layer control law described in Chapter 4 in Yi et al. (2002), which forces the faults to have very similar effects upon the linearized dynamics. The particular conditions of the experiments also played a role, since the faulty radar measurement was still used in the feedback controller. From the viewpoint of the diagnostic system and the sensor measurements, the feedback controller effectively compensated for the fault, although the true range was not equal to the desired spacing.

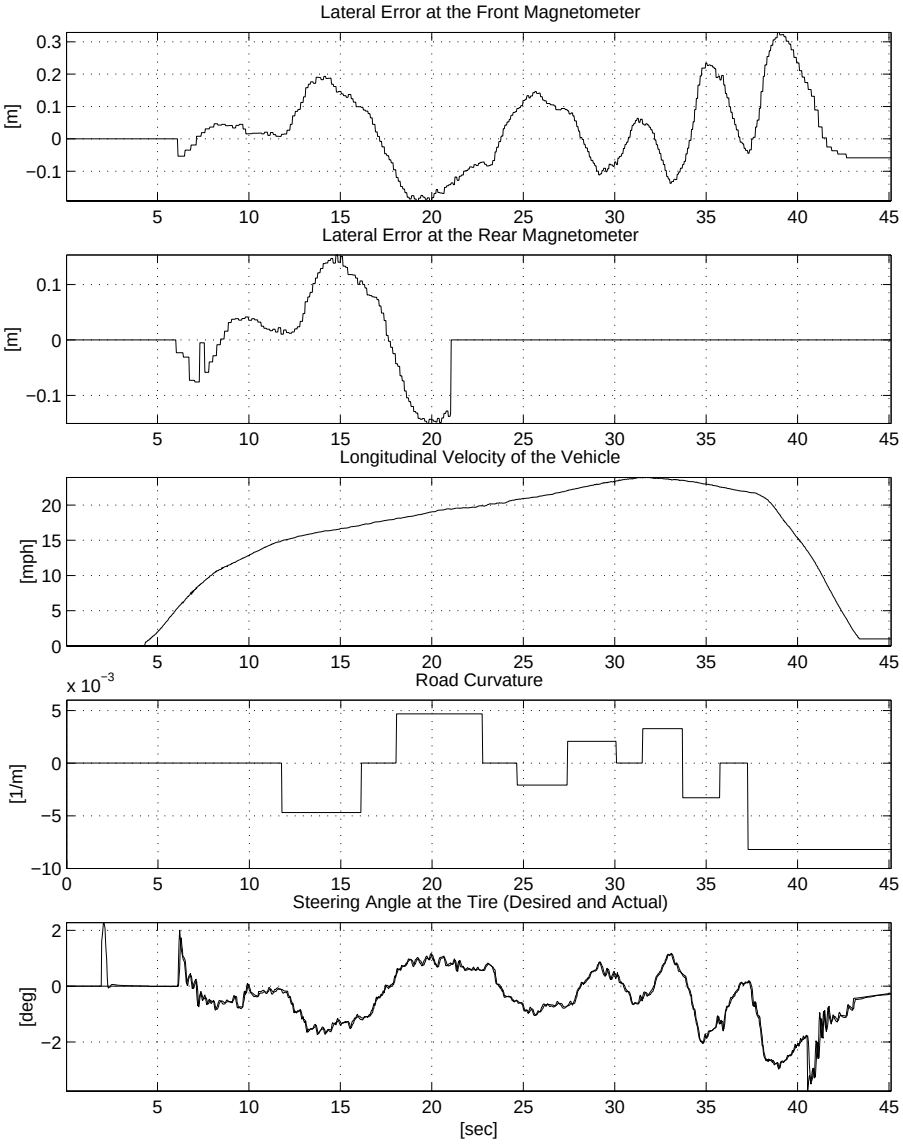

Figure 2.1: Fault #3 in rear magnetometer (around 22 sec): Low Speed (Simultaneous Stabilization Based Controller)

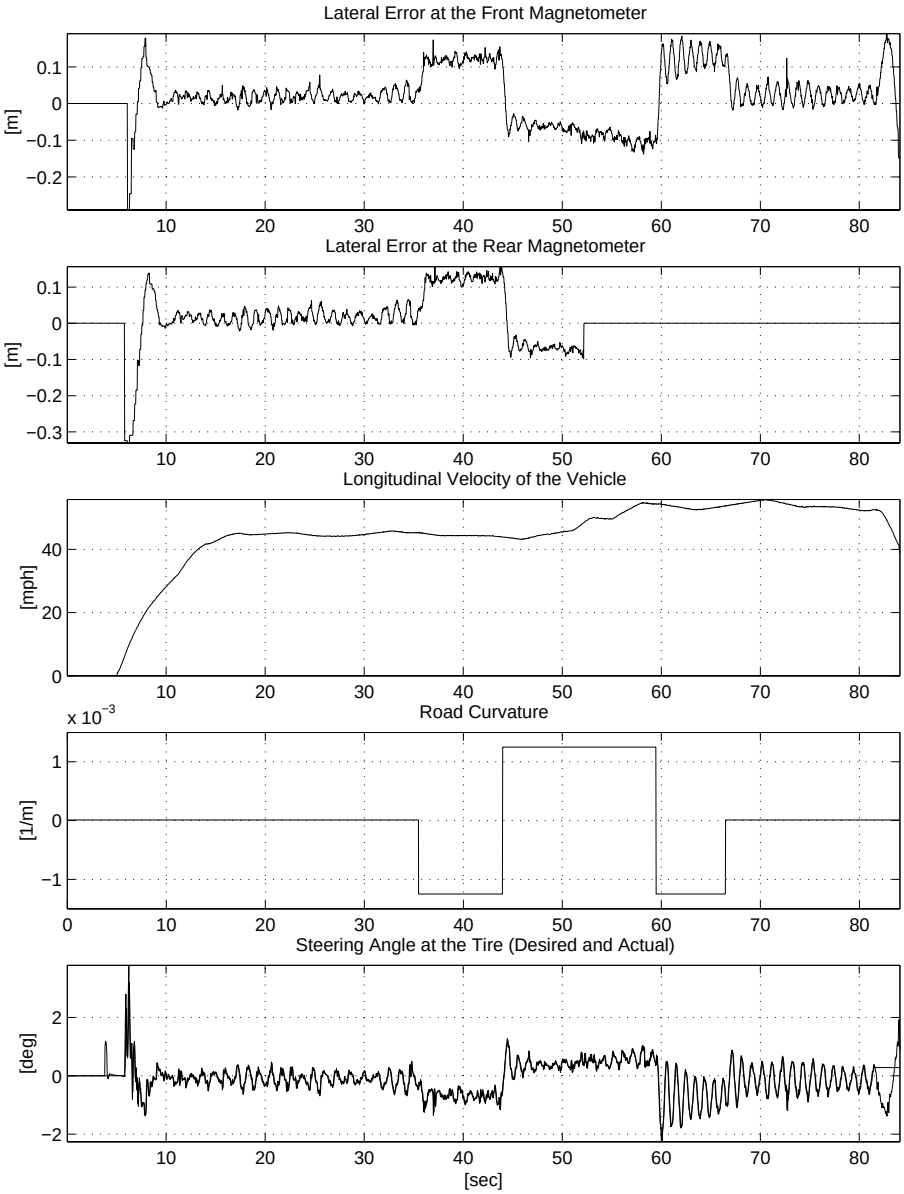

Figure 2.2: Fault #3 in rear magnetometer (around 54 sec): High Speed (Simultaneous Stabilization Based Controller)

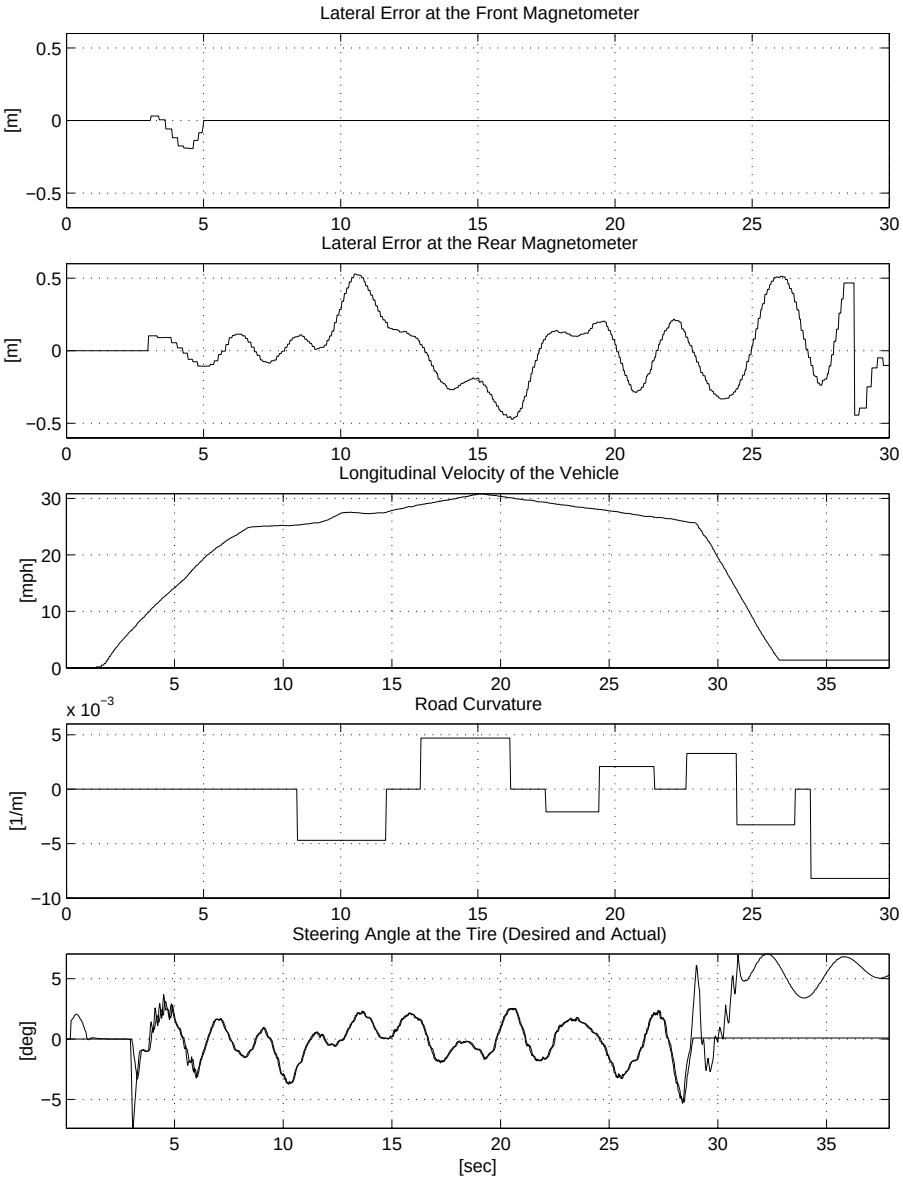

Figure 2.3: Fault #3 in front magnetometer (around 5 sec): Low Speed (Simultaneous Stabilization Based Controller)

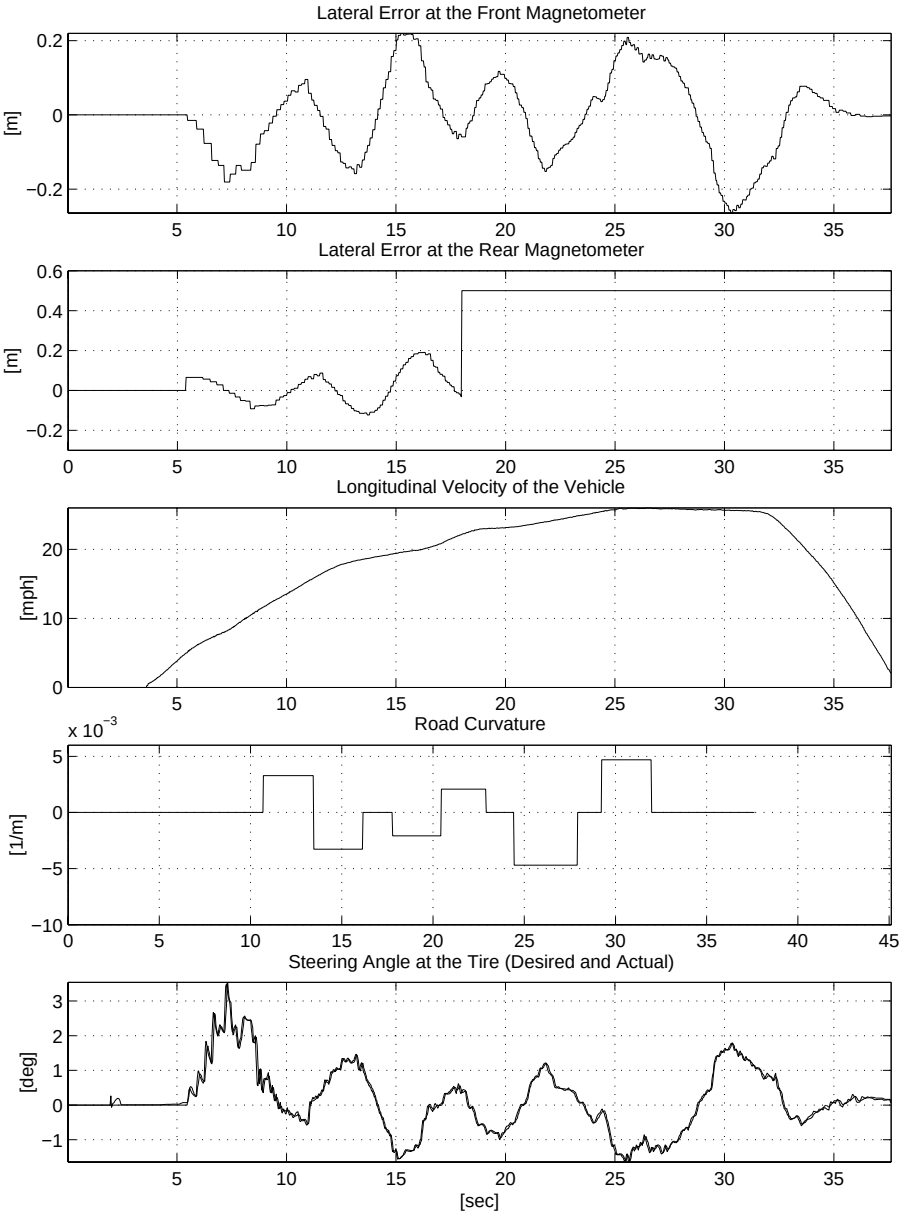

Figure 2.4: Fault #2 in rear magnetometer (around 18 sec): Low Speed (Observer based look-ahead based Controller)

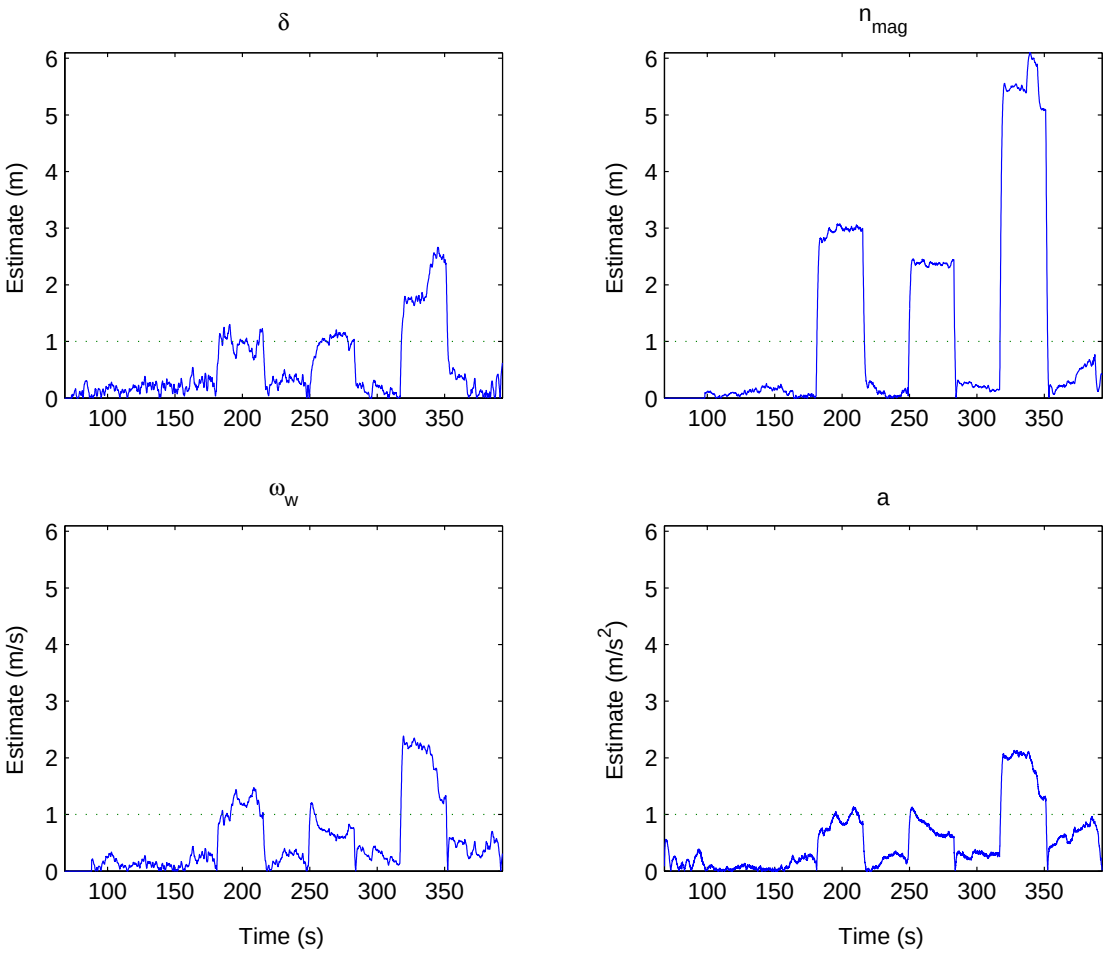

Figure 2.5: Diagnostic system normalized fault mode estimates under a magnetometer fault

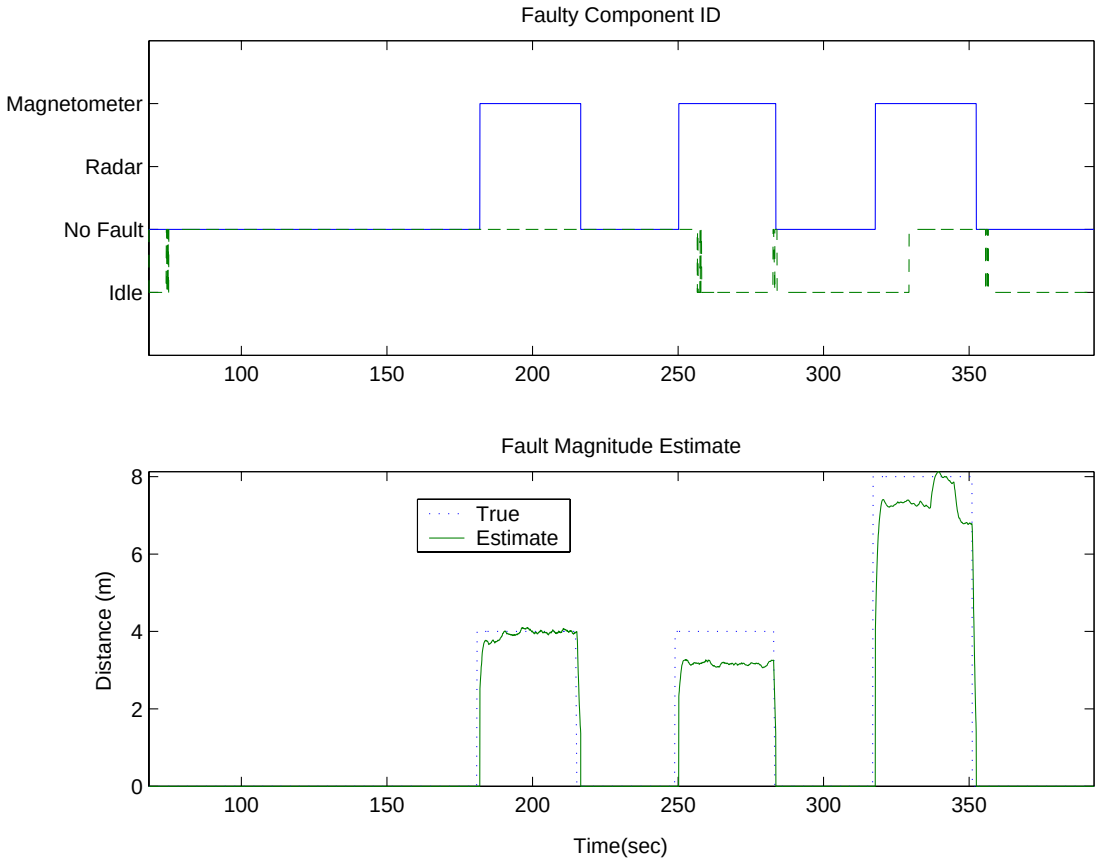

Figure 2.6: Fault identified (top) and fault mode estimate (bottom) under a magnetometer fault

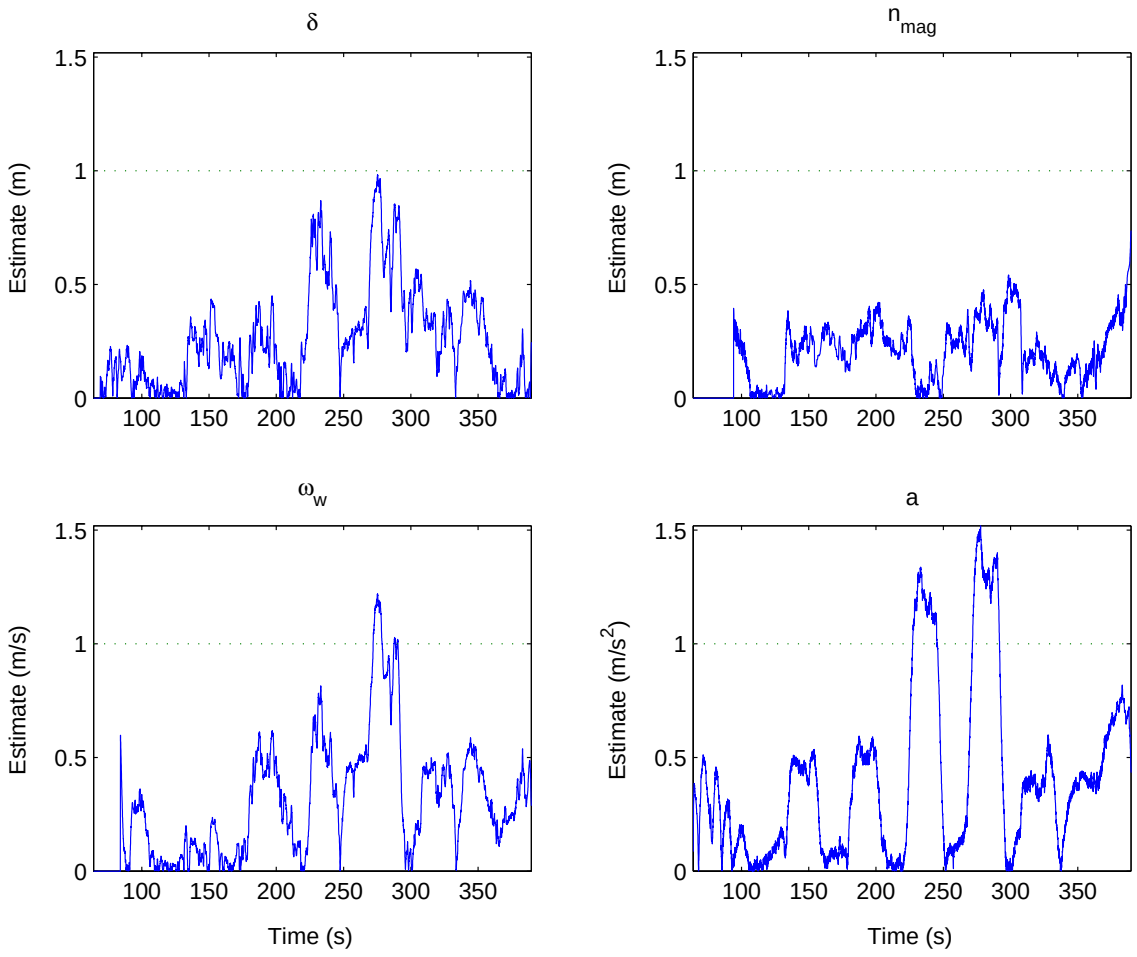

Figure 2.7: Diagnostic system normalized fault mode estimates under a accelerometer fault

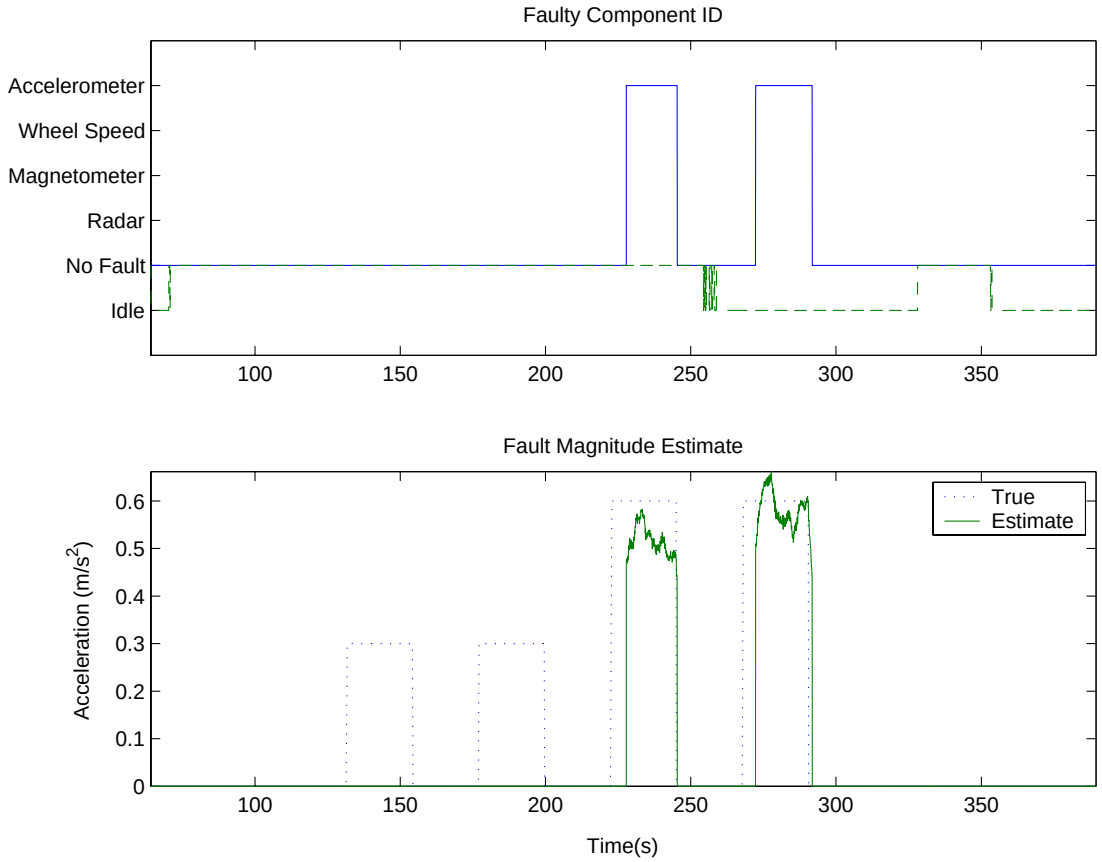

Figure 2.8: Fault identified (top) and fault mode estimate (bottom) under a accelerometer fault

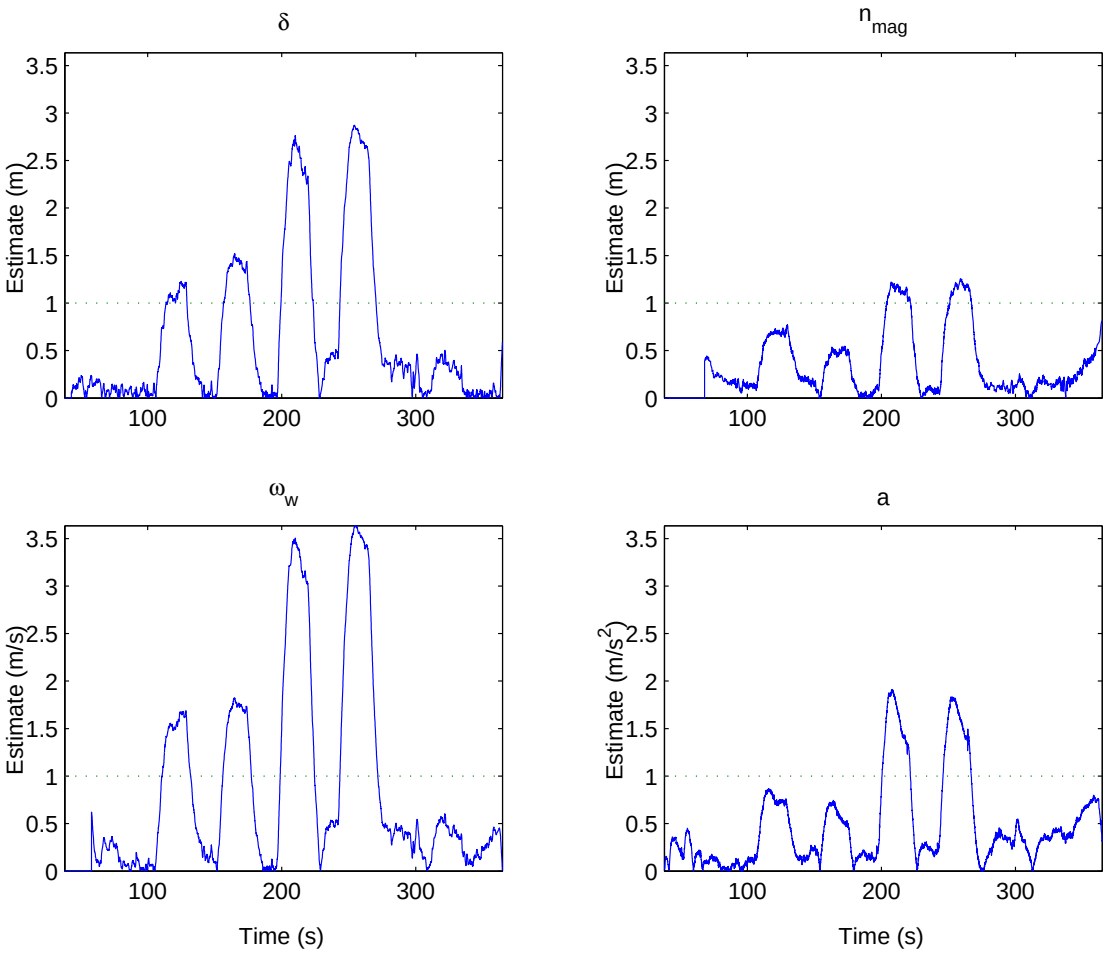

Figure 2.9: Diagnostic system normalized fault mode estimates under a wheel speed sensor fault

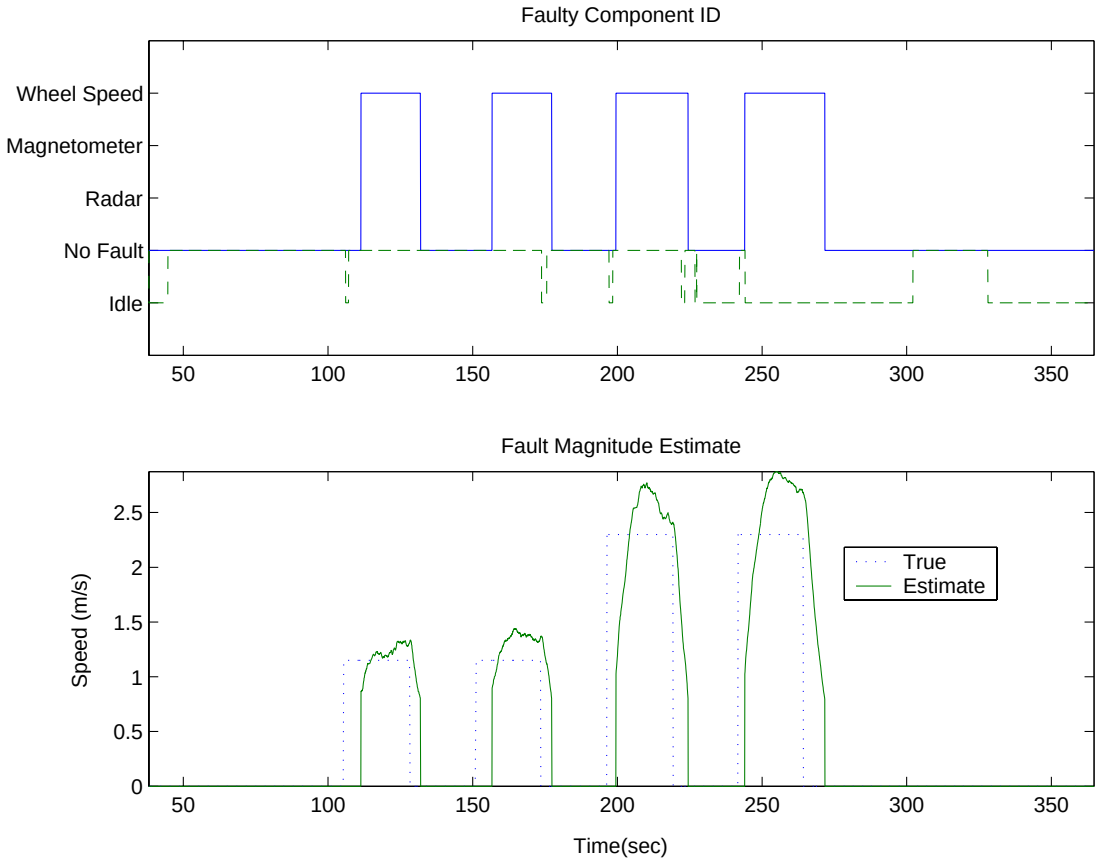

Figure 2.10: Fault identified (top) and fault mode estimate (bottom) under a wheel speed sensor fault

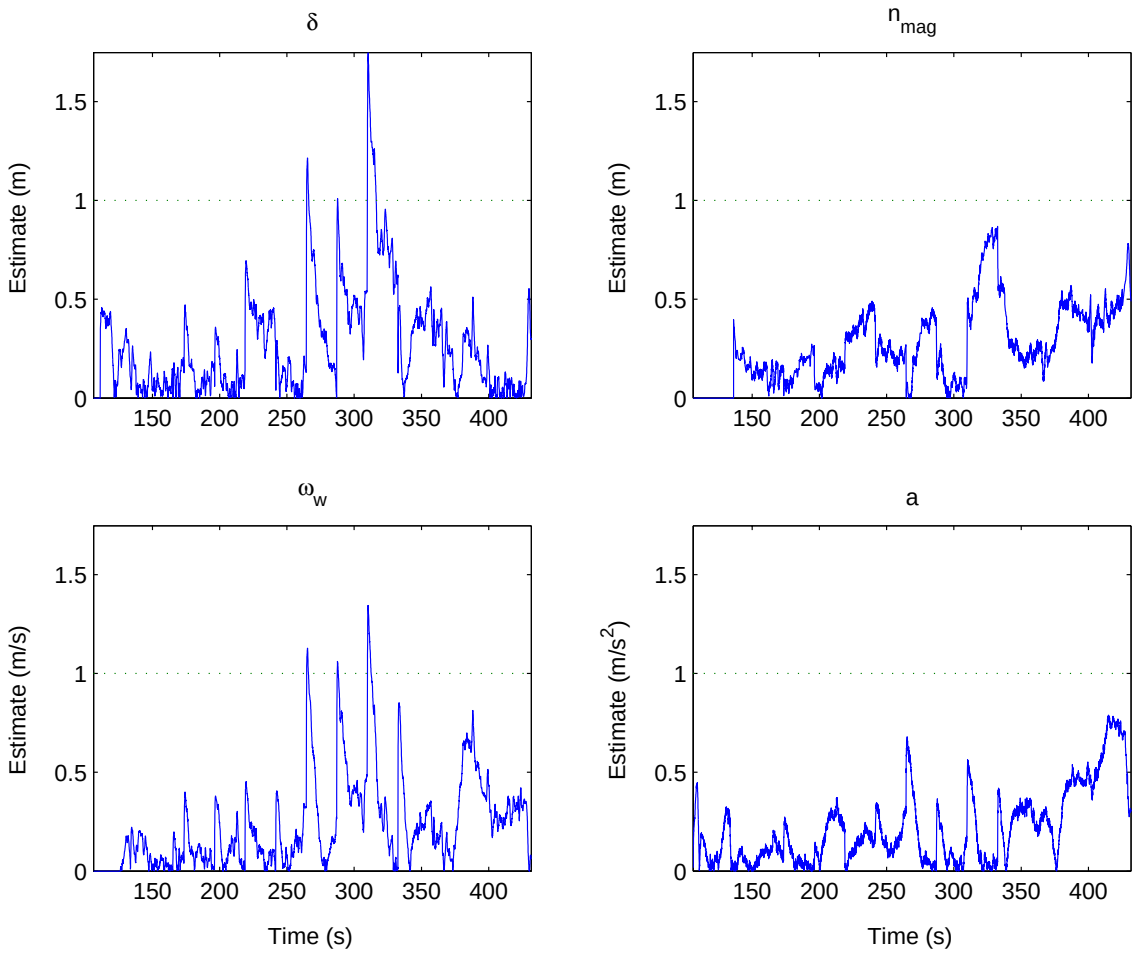

Figure 2.11: Diagnostic system normalized fault mode estimates under a radar fault

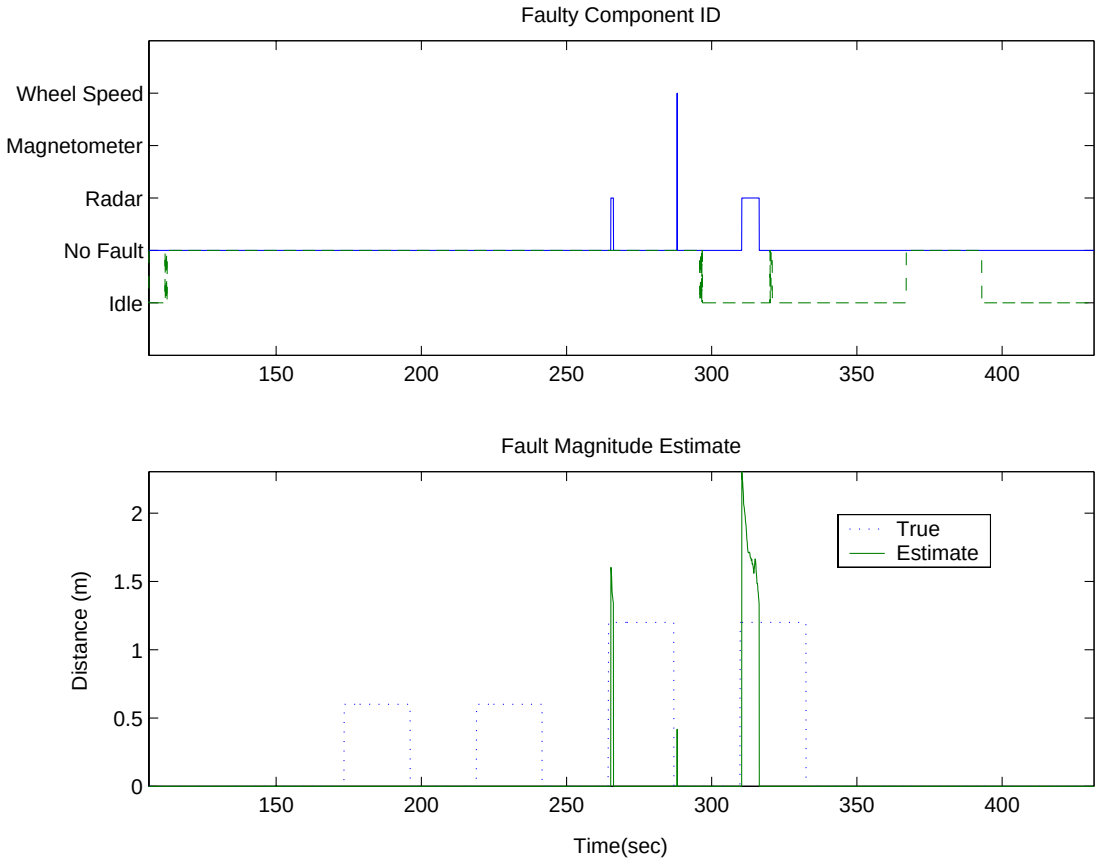

Figure 2.12: Fault identified (top) and fault mode estimate (bottom) under a radar fault

Chapter 3

Soft Fault Diagnostics and Handling — An Extended Dynamic Tire/Road Friction Model

In MOU 373 (Yi et al., 2002), we discussed and developed parameterization approaches to estimate the tire/road friction. The dynamic friction estimation scheme was proposed to determine the characteristics of the tire/road interaction under specific tire and road conditions. However, this method might be insufficient to model the tire/road interactions in reality, because of varying conditions, both on the vehicle side and road side. To model all these variations, it is probably not enough to use only one parameter θ and three parameters σ_i's to capture all the variations occurring at the tire/road interface, respectively, as proposed in Part I of this project report. The multi-parameter estimation schemes using p_i's given in MOU 312 do not yield connections between the parameters (p_i's) and physical variations, such as different road conditions, water depth, tire pressures, etc. Furthermore, these parameters (p_i's) might not converge to their true values due to lack of persistence of excitation of the tire, because slip is small in normal driving situations (slip stays low, even during braking, and hardly reaches 25%). Fortunately, we can still guarantee the underestimation of friction coefficient and slip without emergency maneuvers.

In order to overcome such limitations for the static and dynamic parameterization approaches, in this chapter we propose to extend the dynamic friction model and investigate which varying physical and environmental conditions affect the tire/road friction characteristics. We will explore physical interpretations and focus on the important factors that affect friction characteristics, instead of treating the friction coefficient as a function of several parameters that has little physical meaning. Furthermore, we will investigate the dependencies between the varying conditions and the friction forces, both quantitatively and qualitatively, to enhance current friction identification strategies. Particularly, we will demonstrate two case studies: a three dimensional tire model and a tire model under wet road conditions.

3.1 Hierarchical Perturbation Models

In reality, disturbances, such as different types of road surfaces, rain, or variations in inflation pressure or contact-patch temperature, etc., affect the tire/road friction characteristics. As illustrated in

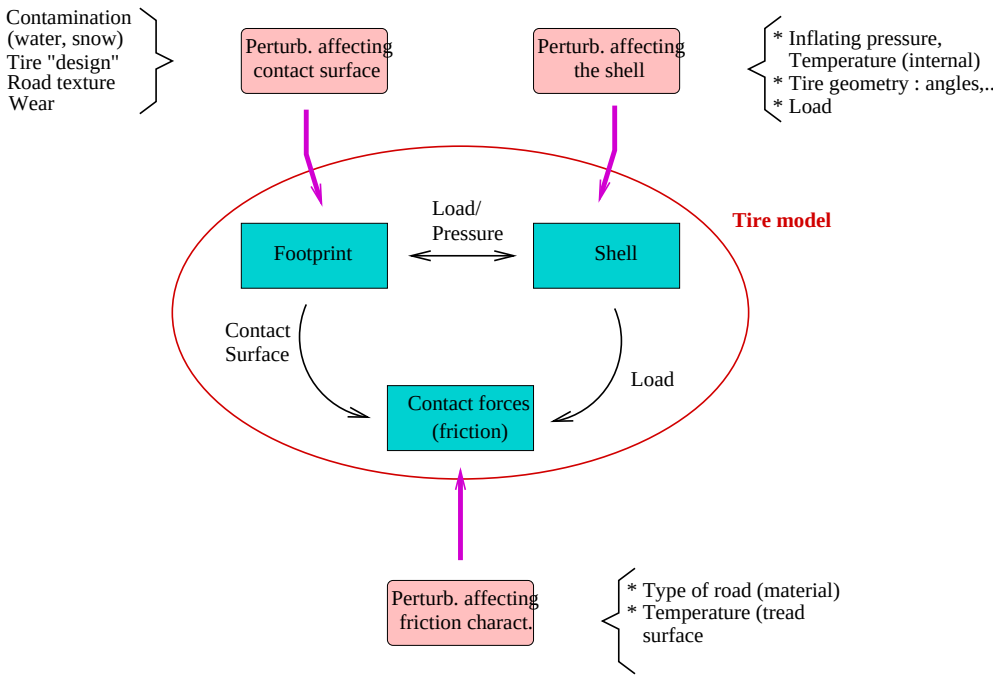

Figure 3.1: A schematic representation underlining the different problems in tire modeling

Fig. 3.1, the external perturbations have a complicated influence on the tire model. Adding extra measurements or specific information about the road or environmental conditions will help to determine the tire/road interaction. To exploit this new idea, a better understanding and comparison of the importance of different perturbation effects on the tire/road interaction is necessary.

Through the literature and numerical experiments, we can classify the physical and environmental perturbations that affect the tire/road interaction into three categories with decreasing importance:

1. **Primary factors**

   - Normal load variation
   - Tire inflating pressure and internal air temperature variations
   - Speed variation (on wet surface)
   - Water depth (when there exists a thick film of water on road)
   - Type of ground surface (wet condition)
   - Tire tread temperature [1]

2. **Secondary factors**

   - Speed (on dry surface)
   - Water depth (when there exists a thin film of water on road)

3. **Other factors**

[1] The influence of tread temperature is important, but not very well known, and we have some difficulty in determining its proper category.

- Type of ground surface (dry condition)

Each of these factors can be analyzed through one or more effects on the following three fundamental parts of the model: the effective contact surface, the effective load, and the friction parameters [2]. For example, we can describe several effects of tire and road conditions, such as wet road conditions, inflation pressure and tread temperature:

- *Wet road condition*, affects mainly the effective contact surface and the effective load on the tire.
- *Tire inflating pressure and internal air temperature variations*, affect mainly the effective contact surface and change the thermodynamic properties of the contact rubber, i.e. friction parameters.
- *Tread temperature variations*, affects the thermodynamic properties of the rubber, i.e. friction parameters.

We believe that one tire or road factor can result in more than one variation of these three fundamental parts of the model, for instance, the tire internal air temperature variation affects both the effective load and friction parameters. Therefore, it is beneficial to introduce these three fundamental parts into the model instead of describing each varying factor individually. Fig. 3.2 illustrates the schematic of such a causal relationship among different factors. As we discussed in Chapter 5 in Yi et al. (2002) most prior work only considered one or two variations of tire and road conditions, due to the complexity of tire/road friction characteristics. Furthermore, even for one or two variations, the analytical or numerical tools that were used, such as analytical mechanics and finite element methods, are complicated. These methods cannot be used for real-time control purposes, or even for vehicle simulations under different conditions. However, we will utilize these prior results for the proposed physical friction model given in Fig. 3.2.

We propose a hierarchical physical tire/road friction model illustrated in Fig. 3.2. The model consists of three layers. We have already discussed the relationships between the varying tire and road conditions and the three fundamental parts that can be included in the nominal friction model [3]. One of the advantages of our proposed scheme is that the modeling structure is flexible and is easily extended to include different variations. Moreover, once we determine the nominal friction model experimentally, we can introduce other variations into the model using analytical and experimental results.

To show a preliminary study of this approach quantitatively, we define the following parameters and states:

1. **Parameters**

   - Road parameters
     - Geometric parameters : texture density ρ_{tx}, amplitude ϵ

[2] We need to describe later those parameters associated with the tire rubber and road pavement, such as Coulomb friction coefficient μ_c, normalized static friction coefficient μ_{st}, Stribeck relative velocity v_s, rubber stiffness σ_0 and damping σ_1 coefficients in the LuGre friction model.

[3] The nominal tire/road friction model can be defined for normal driving conditions. We can then describe different variations on the nominal model. In this sense, it is not very important to precisely define the nominal condition.

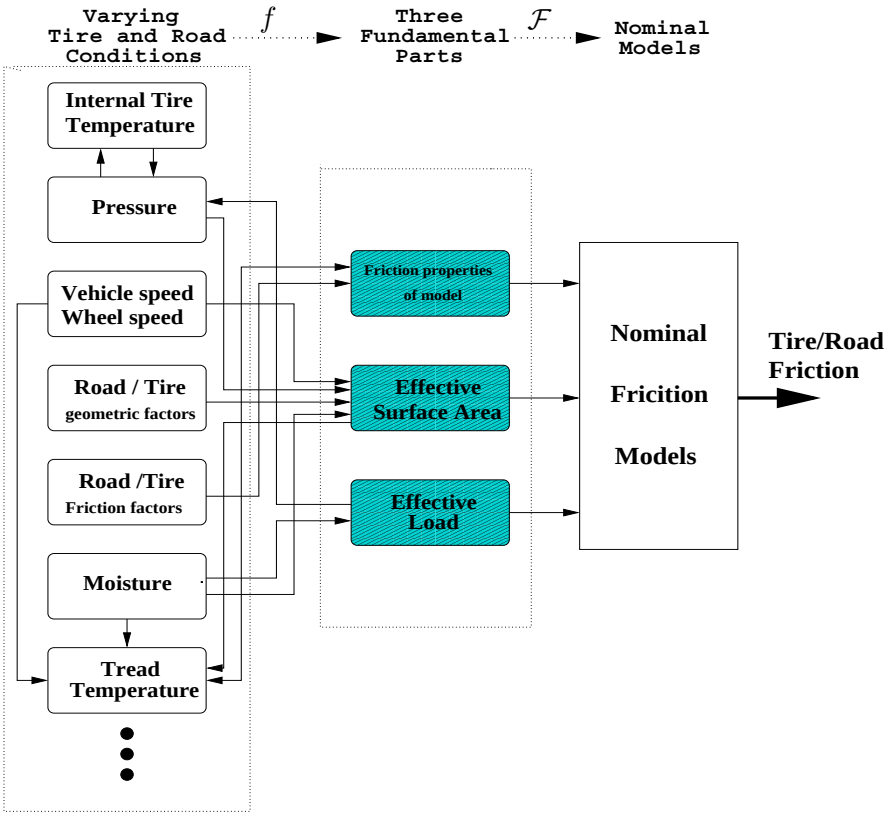

Figure 3.2: A schematic of the physical model scheme (arrow stands for "affects")

  - Friction parameters : fixed for a given surface $\mu_{c_{road}}$
- Tire parameters
  - Geometric parameters : design $\mathcal{D}$, rigidity σ
  - Friction parameters : fixed for a given rubber $\mu_{c_{tire}}$

2. **States**

- Water level for wet road conditions: h_∞
- Normal load: F_z
- Inflation pressure: P, and internal air temperature: T_{in}
- Tread temperature: T_{out}
- Vehicle speed: v
- Wheel speed: ω

Using the above definition of parameters and states, we can write down the map f between the varying tire and road conditions and the three fundamental parts of model (Fig. 3.2) as:

1. **Contact surface variation coefficient** Y_R: describes how different conditions perturb contact surface from nominal conditions. We propose

$$Y_R = f_1(T_{in}, F_z, P, v, \omega, h_\infty, \epsilon, \rho, \sigma, \mathcal{D}) \,.$$

2. **Load variation coefficient** Y_L: summarizes how the load is affected. We propose $Y_L = f_2(Y_R, F_z, h_\infty, \epsilon, \rho, \sigma, \mathcal{D})$.

3. **Friction parameter** Θ: is used to scale the nominal friction characteristics relating only to rubber and pavement properties in the tire model. We propose $\Theta = f_3(\mu_{c_{tire}}, \mu_{c_{road}}, T_{out})$.

We introduce the above mentioned three coefficients ($Y_R,\ Y_L,\ \Theta$) into the nominal friction model, in order to estimate the friction characteristics under different conditions, namely, we consider a map $\mathcal{F}$ from those coefficients to the extended nominal friction model. In the first stage, we will use the dynamic LuGre model in Yi et al. (2002) with $\theta = 1$ as the nominal model. To preliminarily verify the proposed hierarchical model, in this chapter, we study one case that a vehicle is traveling on roads with a thin film water. We first discuss an extension of three dimensional friction model using a LuGre dynamic model.

3.2 3D Dynamic Tire/road Friction Model

This section extends the friction model discussed in Chapter 5 in Yi et al. (2002) by proposing a three dimensional LuGre-type dynamic tire/road friction model. This kind of model is required for new developments in vehicle control design, for example, advanced traction/braking control or advanced steering stability study. In section 3.2.1 we first define the coordinate systems and longitudinal and lateral slips which are used for modeling. A distributed friction model is presented in section 3.2.2 based on the LuGre model and the physical dynamics of the tire. Stationary properties of such a model are also presented. A lumped LuGre model is discussed in section 3.2.4. This lumped friction model is equivalent to the distributed model with certain boundary conditions but is easier to use for estimation and control purposes. Parameter calibration and a comparison with the "magic formula" are included in section 3.2.5.

3.2.1 Slip definitions

In this section we recall the definitions of slip that are commonly used in tire/road friction modeling. We use $v = [v_x, v_y]$ to denote the transitional longitudinal velocity at the center of the contact patch O (see Fig. 3.3) in the wheel plane XOY. The angular velocity of the wheel is denoted by w, v_c is the equivalent wheel transitional velocity at the point O and $v_c = rw$ where r is the radius of the tire. When w is positive (the vehicle is moving forward), the wheel equivalent longitudinal velocity v_c is positive in the coordinate system $\mathcal{R}_0$, where $\mathcal{R}_0$ is defined as a moving frame with velocity v_x with the origin O in the center contact patch.

We define the slip velocity of the point O as $v_s = [v_{sx}, v_{sy}]$ in the wheel plane XOY. The slip angle is denoted by α. The slip ratios used to parameterize the friction model are defined as λ_s and λ_α, for longitudinal and lateral directions, respectively. Two conventions will be used to separate the braking and traction cases (see Fig. 3.3), since as usual, the pseudo-static braking curves are developed under constant velocity whereas pseudo-static traction curves are given for constant angular velocity. These conventions also prevent the slip from becoming undefined when either the wheel speed or the longitudinal speed reach zero.

- In the braking case, longitudinal slip λ_s and lateral slip λ_α are given by

$$\begin{aligned} \lambda_s &= \frac{v_x - v_c}{v_x} = \frac{v_{sx}}{v_x} \\ \lambda_\alpha &= \frac{v_{sy}}{v_x} = |\tan(\alpha)| \end{aligned}$$

  In braking $v_x - v_c > 0$, $v_x \neq 0$, then $1 \geq \lambda_s > 0$.

- In the traction case, longitudinal slip λ_s and lateral slip λ_α are given by

$$\begin{aligned} \lambda_s &= \frac{v_c - v_x}{v_c} = \frac{v_{sx}}{v_c} \\ \lambda_\alpha &= \frac{v_{sy}}{v_c} = (1 - \lambda_s)|\tan(\alpha)| \end{aligned}$$

  In traction, if $v_x - v_c < 0$, $w \neq 0$, then $1 \geq \lambda_s > 0$.

Other conventions, like those used for the "magic formula", can easily be employed and do not change the final results. In this particular case, a specific definition needs to be considered when the longitudinal speed v_x or v_c tend to zero, in order to prevent a singularity in the definition of the slips.

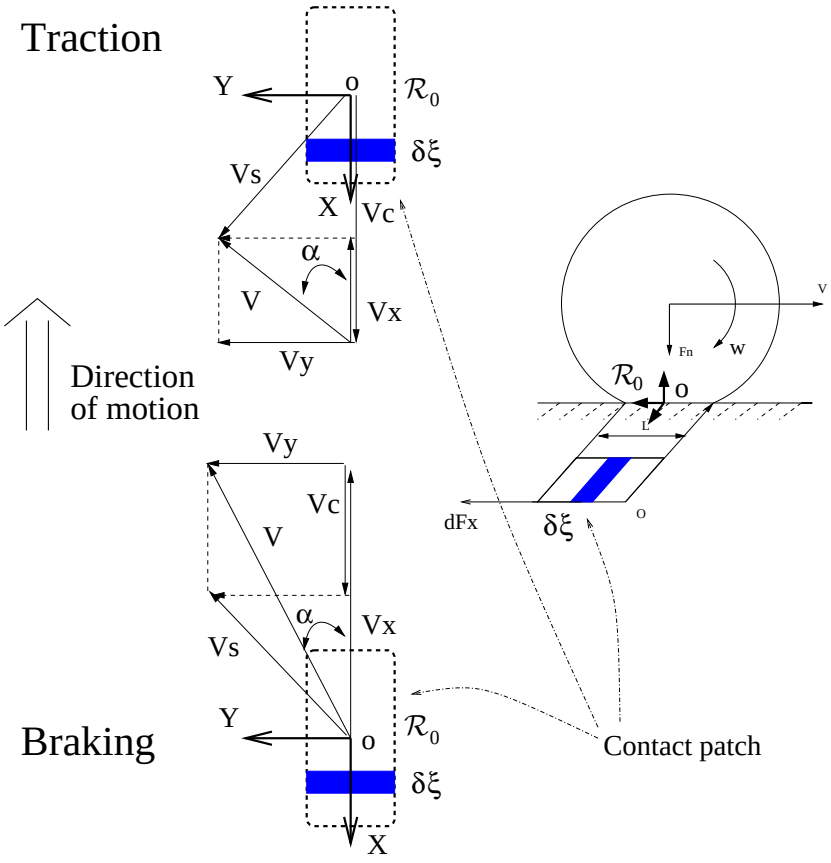

Figure 3.3: Convention for the slip definition for both braking and traction cases

3.2.2 Distributed dynamic tire/road friction model

In this section we propose to extend the models to consider both longitudinal and lateral motions, and investigate the resulting forces and torque at the center of the contact patch.

Friction forces

Let $\delta\xi$ represent a small slice of the deformed belt crossing the contact patch at position ξ in coordinate $\mathcal{R}_0$ frame (see Fig. 3.3). The slice $\delta\xi$ is moving at the speed $v_{\delta\xi} = [v_x, v_y + \xi\dot{\varphi}]$ with $\dot{\varphi}$ the yaw speed of the rim (Sorine and Szymanski, 2000). We can model the dry friction in each slice using the LuGre dynamic friction model. The contact between the two surfaces can be represented by microscopic bristle deflections with the coordinates $\delta z(\xi, t) = [\delta z_x(\xi, t), \delta z_y(\xi, t)]$, and the relative velocity of each slice at ξ with respect to O is given as $v_r(\xi, t) = [v_{rx}(\xi, t), v_{ry}(\xi, t)] = [-v_{sx}(t), -v_{sy}(t) - \xi\dot{\varphi}]$ (the direction of the total force is opposite to the slip vector). However, we treat the tire belt as a rigid body [4].

For the rigid tire belt model, the extended two dimensional distributed tire/road friction model is given by

$$\delta\dot{z}_x(\xi, t) = v_{rx} - \frac{\sigma_{0_x}}{h_x(v_{rx})}\delta z_x(\xi, t)|v_{rx}| \tag{3.1a}$$

$$\delta\dot{z}_y(\xi, t) = v_{ry} - \frac{\sigma_{0_y}}{h_y(v_{ry})}\delta z_y(\xi, t)|v_{ry}| \tag{3.1b}$$

and the friction forces

$$\delta F_x = \left[\sigma_{0_x}\delta z_x(\xi, t) + \sigma_{1_x}\delta\dot{z}_x(\xi, t) + \sigma_{2_x}v_{rx}\right]\delta F_z \tag{3.2a}$$

$$\delta F_y = \left[\sigma_{0_y}\delta z_y(\xi, t) + \sigma_{1_y}\delta\dot{z}_y(\xi, t) + \sigma_{2_y}v_{ry}\right]\delta F_z\,, \tag{3.2b}$$

where σ_{j_i}, $i = x, y$; $j = 0, 1, 2$, are the dynamic coefficients of the LuGre friction model for lateral and longitudinal directions, known as the normalized rubber stiffness (σ_{0_i}), the normalized rubber damping (σ_{1_i}), and the normalized viscous relative damping (σ_{2_i}). The normal load δF_z is considered uniformly distributed over the patch along ξ direction, thus $\delta F_z = F_z/L$, and

$$h_x(v_{rx}) = \mu_{c_x} + (\mu_{st_x} - \mu_{c_x})e^{-|\frac{v_{rx}}{v_{s_x}}|^{1/2}} \tag{3.3a}$$

$$h_y(v_{ry}) = \mu_{c_y} + (\mu_{st_y} - \mu_{c_y})e^{-|\frac{v_{ry}}{v_{s_y}}|^{1/2}} \tag{3.3b}$$

are two functions that characterize the steady-state properties of the friction, where μ_{c_i}, μ_{st_i}, v_{s_i} are, respectively, the Coulomb friction coefficient, the normalized static friction and the Stribeck relative velocity. The two LuGre models for longitudinal and lateral motions use different parameters since the friction properties of the contact tire/road are different in longitudinal and lateral directions. The fact that the tire has non-isotropic properties is well known and has already been introduced in most current models (Bakker et al., 1987; Burckhardt, 1987).

[4] The model might be extended in order to include dynamic properties of the rubber belt. In this case, the longitudinal velocity of each slice $v_{\delta\xi}$ of the contact patch would have a more complex expression that might include camber angle dependencies or other factors. These notions have already been explained in the literature (Sorine and Szymanski, 2000; Gim and Nikravesh, 1990).

The system given in Eqs. (3.1) and (3.2) is both time and space dependent, and as a consequence the full derivative of $\delta z_i(\xi,t)$, $i = x, y$, for longitudinal and lateral directions is given by

$$\delta \dot{z}_i(\xi,t) = \frac{\partial \delta z_i(\xi,t)}{\partial \xi}\frac{\partial \xi}{\partial t} + \frac{\partial \delta z_i(\xi,t)}{\partial t}\,. \tag{3.4}$$

The system composed of (3.1), (3.2) and (3.4) is difficult to solve analytically. However, the pseudo-static case (v_x and ω constant) can be studied and compared with the available tire models in this research area. This will be discussed in section 3.2.3.

Self-aligning torque

The self-aligning torque is an important part of the tire model because the reaction force applied to the vehicle (steering wheel feedback force) is strongly dependent upon it. The self-aligning torque consists of two important elements, the yaw motion of the tire that creates a friction torque $\delta M_{z_1}(\xi,t)$, and the moment of the friction forces about the center of wheel frame $\delta M_{z_2}(\xi,t)$. Both of these effects generate the torque at the center of patch, known as the self-aligning torque. In current studies we neglect the yaw motion of the tire $\delta M_{z_1}(\xi,t)$, due to the fact that the yaw motion effect is small (Sorine and Szymanski, 2000). Denoting φ as the yaw angle, this torque could easily be described by using a third dynamic friction model similar to the LuGre model given in section 3.2.2 (Eqs. (3.5) and (3.6)). Given a yaw bristle deformation,

$$\delta \dot{z}_z(\xi,t) = \dot{\varphi} - \frac{\sigma_{0_z}}{h_z(\varphi)}\delta z_z(\xi,t)|\dot{\varphi}|\,, \tag{3.5}$$

where δz_z is the deformation to generate friction torque δM_z. The friction torque could be expressed by the following equation

$$\delta M_{z_1} = \left[\sigma_{0_z}\delta z_z(\xi,t) + \sigma_{1_z}\delta \dot{z}_z(\xi,t) + \sigma_{2_z}\dot{\varphi}\right]\delta F_z\,. \tag{3.6}$$

The tire/road forces and torque are always calculated at the center of the patch O in Fig. 3.3. Consequently, a self-aligning torque is produced resulting from the non-symmetry of the contact patch deformation $\delta z(\xi,t)$, or forces $\delta F_y(\xi,t)$, over the contact patch length L. The equivalent forces and torque produced by a slice $\delta\xi$ at position ξ with respect to the center of the patch O is given by $[\delta F_x, \delta F_y, \delta M_z = \xi \delta F_y]$ and the total tire/road interaction in the patch center is now expressed by two forces F_x, F_y and the self-aligning torque M_z:

$$F_x = \int_{-\frac{L}{2}}^{\frac{L}{2}} \delta F_x(\xi,t)d\xi \tag{3.7a}$$

$$F_y = \int_{-\frac{L}{2}}^{\frac{L}{2}} \delta F_y(\xi,t)d\xi \tag{3.7b}$$

$$M_z = \int_{-\frac{L}{2}}^{\frac{L}{2}} [\underbrace{\delta M_{z_1}(\xi,t)}_{\text{neglected}} + \delta M_{z_2}(\xi,t)\,]d\xi = \int_{-\frac{L}{2}}^{\frac{L}{2}} \xi \delta F_y(\xi,t)d\xi \tag{3.7c}$$

Remark 3.1 Eventually, we could also look for the non-symmetric force distribution along the width of the patch and add other components to the model. In particular, the self-aligning torque will then depend upon the longitudinal force $\delta F_x(\xi,t)$ as confirmed by the experiments.

3.2.3 Stationary properties

The stationary characteristics of the tire are widely applied in this research area. To produce these characteristics, a complex experimental setup is usually utilized. These conditions are hard to obtain on a real vehicle, since the required maneuvers would be very severe for the passengers. Each point on the stationary curve is given for a constant slip and a constant wheel velocity or wheel angular velocity, therefore v_c and V remain constant and a slip angle α is obtained. The yaw motion of the rim is also not considered, i.e. $\dot{\varphi} = 0$. Therefore, during the stationary conditions, ξ and t are no longer independent because of constant velocity, thus we have $\delta z_i(\xi, t) = \delta z_i(t)$ if we desire a time varying solution, or $\delta z_i(\xi, t) = \delta z_i(\xi)$ if we require a spatial solution. We choose to calculate the spatial solution in the frame $\mathcal{R}_0$ defined previously. Notice that, if $\dot{\xi} = v_c$ is constant during stationary traction conditions, we have

$$\frac{d}{dt}\delta z_i(\xi, t) = \frac{d\delta z_i(\xi)}{d\xi}\frac{d\xi}{dt} = \frac{d\delta z_i(\xi)}{d\xi}v_c, \quad i = x, y$$

with spatial coordinates. As a consequence, the stationary bristle model with spatial coordinates becomes

$$\frac{d\delta z_i(\xi)}{d\xi}v_c = -v_{si} - \frac{\sigma_{0_i}}{h_i(v_{si})}\delta z_i(\xi)|v_{si}|$$

with $\delta z_i\left(-\frac{L}{2}\right) = 0$ as the boundary condition. The spatial solution is given by

$$\delta z_i(\xi) = \operatorname{sign}(-v_{si})\frac{h_i(v_{si})}{\sigma_{0_i}}\left[1 - e^{-\frac{\sigma_{0_i}|v_{si}|/v_c}{h_i(v_{si})}(\xi+\frac{L}{2})}\right].$$

Integrating the forces and torque along the contact patch using the formula (3.7), we obtain three components for the stationary tire model F_x, F_y, M_z for the traction case:

$$\frac{F_x}{F_z} = -\gamma_x(v_{sx})\operatorname{sign}(v_{sx})h_x(v_{sx})\left[1 + \frac{h_x(v_{sx})}{L\sigma_0\lambda_s}(e^{-\frac{\sigma_{0_x}L\lambda_s}{h_x(v_{sx})}} - 1)\right] - (\sigma_{1_x} + \sigma_{2_x})v_{sx} \tag{3.8a}$$

$$\frac{F_y}{F_z} = -\gamma_y(v_{sy})\operatorname{sign}(v_{sy})h_y(v_{sy})\left[1 + \frac{h_y(v_{sy})}{L\sigma_{0_y}\lambda_\alpha}(e^{-\frac{\sigma_{0_y}L\lambda_\alpha}{h_y(v_{sy})}} - 1)\right] - (\sigma_{1_y} + \sigma_{2_y})v_{sy} \tag{3.8b}$$

$$\frac{M_z}{F_z} = -\frac{\gamma_y(v_{sy})\operatorname{sign}(v_{sy})h_y^2(v_{sy})}{2\sigma_{0_y}^2\lambda_\alpha}\left[(e^{-\frac{\sigma_{0_y}L\lambda_\alpha}{h_y(v_{sy})}} - 1) + \frac{2h_y(v_{sy})}{L\sigma_{0_y}\lambda_\alpha}\left(e^{-\frac{\sigma_{0_y}L\lambda_\alpha}{h_y(v_{sy})}} - 1\right)\right] \tag{3.8c}$$

The function γ_i defined as $\gamma_i(v_{s_i}) = 1 - \frac{\sigma_{1_i}|v_{s_i}|}{h_i(v_{s_i})}$, for $i = x, y$. Calibration of parameters and comparison with the "magic formula" are presented later in section 3.2.5. For the braking case, we can find similar formulae for F_x, F_y, and M_z.

3.2.4 Lumped dynamic tire/road friction model

Distributed models are difficult to use for estimation and control purposes. Thus, we will now develop a simplified lumped parametric representation. An approach has been given in Canudas de Wit and Tsiotras (1999) for a traction case and in Yi et al. (2002) for a braking case, assuming vanished boundary conditions for the deformation of contact patch if the deformation is symmetric with

respect to the center of the patch O. If we relax this assumption with non-symmetric deformation of the patch, we can compute a similar 3D lumped friction model same as Deur et al. (2001). In this paper, we obtain the lumped model by defining lumped variables $\bar{z}_i$ as follows,

$$\bar{z}_i(t) = \frac{1}{L}\int_{-\frac{L}{2}}^{\frac{L}{2}} \delta z_i(\xi,t)d\xi, \qquad i = x, y\,.$$

Neglecting the yaw motion of the rim, i.e. $\dot{\varphi} = 0$, the distributed friction model becomes

$$\dot{\bar{z}}_i + \int_{-\frac{L}{2}}^{\frac{L}{2}} \frac{\partial \xi}{\partial t}\frac{\partial \delta z_i(\xi,t)}{\partial \xi}d\xi = -v_{si} - \frac{\sigma_{0_i}}{h_i(v_{si})}\bar{z}_i|v_{si}|\,, \tag{3.9}$$

where $\frac{\partial \xi}{\partial t} = v_c$ is assumed uniformly along the patch and $i = x, y$. Assuming $\delta z\left(-\frac{L}{2}, t\right) = 0$, the system turns into two first order differential equations which are similar to those in Yi et al. (2002) ($\delta z(\frac{L}{2}, t) \neq 0$ because the solution is not symmetric). Finally the lumped model can be defined by

- **Internal states**

$$\delta\dot{z}_i\left(\frac{L}{2}, t\right) = -v_{si} - \frac{\sigma_{0_i}}{h_i(v_{si})}\delta z_i\left(\frac{L}{2}, t\right)|v_{si}|$$
$$\dot{\bar{z}}_i + r\omega\delta z\left(\frac{L}{2}, t\right) = -v_{si} - \frac{\sigma_{0_i}}{h_i(v_{si})}\bar{z}_i|v_{si}|$$

  with $\bar{z}_i(0) = 0$ and $\delta z\left(\frac{L}{2}, 0\right) = 0$.

- **Lumped forces**

$$F_i = \left[\sigma_{0_i}\bar{z}_i + \sigma_{1_i}\dot{\bar{z}}_i + \sigma_{2_i}v_{r_i}\right]F_z, \quad i = x, y.$$

Using the new lumped internal states $\bar{z}_i$ and $\delta z_i\left(\frac{L}{2}, t\right)$, we can calculate self-aligning torque as follows:

- **Lumped self-aligning torque**

$$M_z = \int_{-\frac{L}{2}}^{\frac{L}{2}} \xi\delta F_y(\xi,t)d\xi$$

  Noticing that

$$\begin{aligned}
\frac{\partial \delta F_y}{\partial t} &= \frac{F_z}{L}\left[\sigma_{0_y}\gamma_y(v_{sy})\frac{\partial \delta z_y(\xi,t)}{\partial t} + \sigma_{y_0}\dot{\gamma}_y(v_{sy})\delta z_y(\xi,t) + (\sigma_{1_y} + \sigma_{2_y})\dot{v}_{ry}\right] \\
&= \frac{F_z}{L}\left[\sigma_{y_0}\gamma_y(v_{sy})\left(v_{sy} - \frac{\sigma_{0_y}|v_{sy}|}{h_y(v_{sy})}\delta z_y(\xi,t)v_c\frac{\partial \delta z_y(\xi,t)}{\partial \xi}\right)\right. \\
&\quad \left. +\sigma_{0_y}\dot{\gamma}_y(v_{sy})\delta z_y(\xi,t) + (\sigma_{1_y} + \sigma_{2_y})\dot{v}_{ry}\right]\,,
\end{aligned}$$

  we have

$$\begin{aligned}
\dot{M}_z &= \int_{-\frac{L}{2}}^{\frac{L}{2}}\left[\dot{\xi}\delta F_y(\xi,t) + \xi\frac{\partial \delta F_y(\xi,t)}{\partial t}\right]d\xi \\
&= v_c F_y + \left(\frac{\dot{\gamma}_y(v_{sy})}{\gamma_y(v_{sy})} - \frac{\sigma_{0_y}|v_{sy}|}{h_y(v_{sy})}\right)M_z + \sigma_{0_y}\gamma_y(v_{sy})v_c\left(\bar{z}_y - \frac{\delta z_y(\frac{L}{2}, t)}{2}\right)F_z
\end{aligned}$$

Remark 3.2 The dynamic tire/road friction model has several interesting properties:

1. The model is an average over the patch length and depends only upon time.
2. The model is not limited to stationary curves, we can describe the system when v_c and v are not constant.
3. The bristle dynamics are relatively fast with respect to vehicle dynamics when slip velocity v_s is large. However, for small values of the slip velocities v_{sx} and v_{sy}, the friction dynamics become slower and should be considered in vehicle control and simulations.

3.2.5 Parameter calibration and numerical examples

We need to calibrate the dynamic friction model parameters before the model can be used for friction estimation and vehicle control. Moreover, we should validate the model with experimental data. In this section, we use the typical tire model $165\text{-}65\mathrm{R}14$ as an example. The "magic formula" has been calibrated for dry surface conditions for tires given by Michelin Inc. under a pure braking/corning maneuver. Fig. 3.4 shows the test results from the calibrated "magic formula".

We calibrated the parameters of our model using the nonlinear curve-fitting methods in MATLAB. The model parameters are given in Table 3.1 and the force and torque curves in Fig. 3.4. The result shows a good fit between the model prediction and the empirical models. Moreover, we found that combining the lateral force F_y and the self-aligning torque M_z can help the determination of some parameters, such as model parameters in the lateral direction.

Table 3.1: Friction parameters for F_x and F_y

Coefficients	$i = x$	$i = y$
$\sigma_{0_i}\,(N/m)$	267	122
$\sigma_{1_i}\,(Nsec/m)$	1.33	0.327
$\sigma_{2_i}\,(Nsec/m)$	0.0001	0
μ_{c_i}	0.57	0.2675
μ_{st_i}	1.41	3.05
$v_{s_i}\,(m/sec)$	2.66	1.17

3.3 Tire/road Friction Model Under Wet Road Conditions

In this section, we use the approach discussed in section 3.1 to study a tire/road friction model under wet road conditions.

3.3.1 Background

Road conditions have a tremendous effect on the tire behavior. The depth of water on the road greatly influences tire/road friction. These phenomena are complex and related to the different aspects of

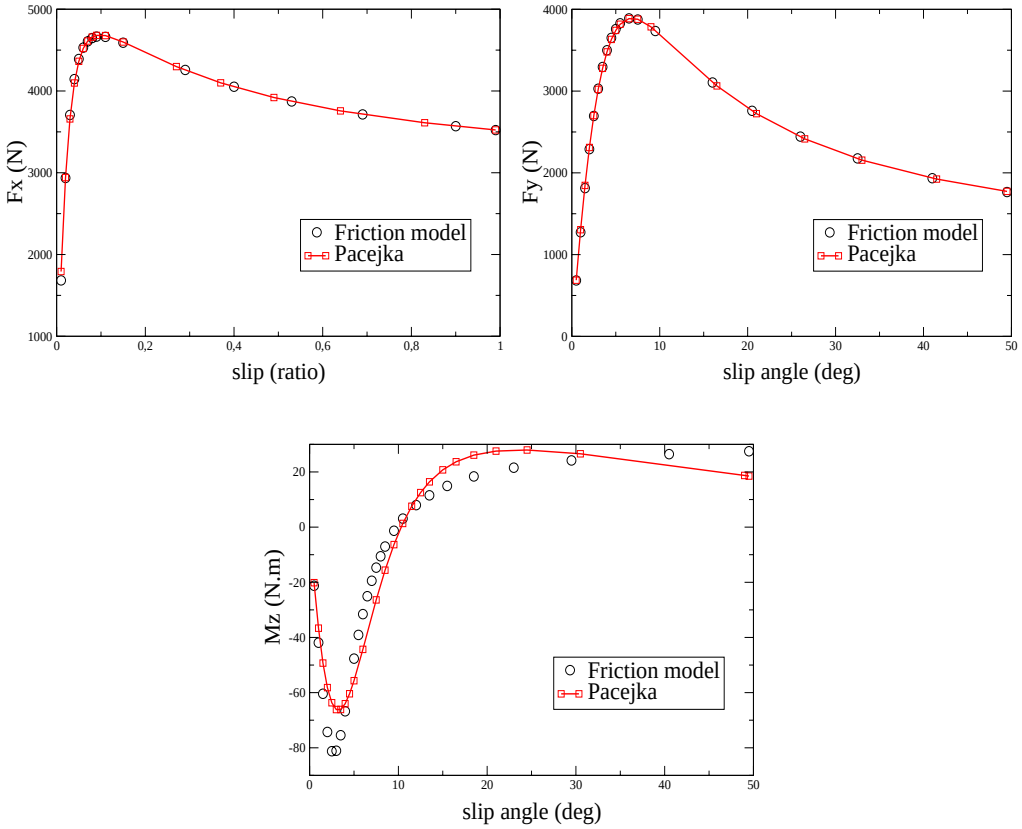

Figure 3.4: Comparisons of the stationary tire/road friction model and the "magic formula" (braking case with $v = 15m/s$)

the contact patch between the tire and the road. Previous analysis made use of different water level categories such as thin or thick film of water on the road (Browne and Whicker, 1977; Rohde, 1977; Rohde, 1975). Even if the distinction between these two situations sounds artificial, it helps in understanding the contamination of the tire/road contact patch by water. In the limiting situation of a thin water layer, the contact between tire and road is completely lost due to full contamination of the interface [5]. This problem is called viscous hydro-planing (Pottinger and Yager, 1985; Moore, 1964). On the other hand, for a thick water layer, an extra force is generated in front of the tire due to the accumulation of water (hydro-dynamic forces). In this situation, the contact between the two surfaces could be lost. This phenomenon is named dynamic hydro-planning. The last case is more general than viscous hydro-planing due to the fact that other hydro-dynamical effects take place during the contact process.

Consequently, we can summarize these remarks as follows: for every set of experimental conditions in wet weather, there exists a definite velocity called the hydro-planing limit, beyond which hydro-planing occurs (see Moore (1964)). At this velocity, the wheel is in general supported by:

- A hydro-dynamic upward thrust, just ahead of the contact area of the tire. The magnitude of this force is determined by the water layer depth h_∞ (for thick films) and vehicle velocity v.

[5] When water has invaded the complete contact area between the tire and ground.

An expression for the upward thrust, F_H, can be found in (Moore, 1964). It has been shown to depend upon v^2, where v is the velocity of the vehicle:

$$F_H = \varsigma \varpi(h_\infty) v^2 F_z = Y_F F_z \,, \tag{3.11}$$

where Y_F is a ratio, defined as a function of a constant ς, the normal load F_z, and a geometric angle ϖ, which is a function of the road water level h_∞:

$$\varpi = \sqrt{\left(\frac{L}{2r}\right)^2 - \left(\frac{h_\infty}{r}\right)^2 + \frac{2h_\infty}{r}\sqrt{1-\left(\frac{L}{2r}\right)^2}} - \left(\frac{L}{2r}\right) . \tag{3.12}$$

- A squeezed film and wiping effect in the contact area. The squeezed film effect is due to the inability of the tread elements traversing the contact area to remove the last few tenths of a millimeter of water in the available time. The wiping effect is due to the longitudinal and lateral relative motion of the tire elements in the contact area.

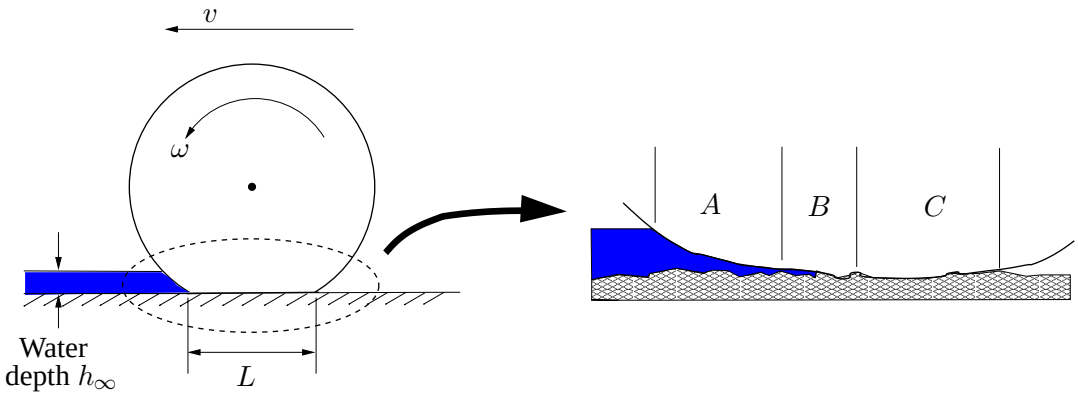

Figure 3.5: Tire footprint under wet road conditions

Remark 3.3 F_H approaches the load of the wheel at high velocities (over $200km/h$, which is not realistic) depending of the amount of water h_∞ on the road. Thus, as stated before, the hydro-dynamic thrust F_H is not the only factor contributing to hydro-planing. This discrepancy is due to variations in the contact area due to a thin film of water squeezed at the tire/road interface: the thin water layer supports a fraction of the load of the wheel, and hence the effective contact area and the effective normal load decreases.

The inclusion of all of these effects in the tire model is possible if we can develop dynamic expressions for the contact patch and the effective load of the tire, based on physic laws. Determining the contact patch is a difficult problem, and several empirical or semi-empirical approaches have been proposed in the literature (Horne and Buhlmann, 1983; Pottinger and Yager, 1985). In these references, the road/tire interface (contact area) is divided into three areas (see Fig. 3.5):

1. Zone A – sinkage zone: Under wet road conditions, the forward part, normally considered the contact area under dry conditions, floats on a thin film of water, and the thickness decreases progressively as individual tread elements traverse the contact area. Since the tire, water-film and surface have no relative motion in the contact area, the problem is a buoyancy calculation.

2. Zone B – transition zone: This zone occupies a relatively small section of the contact area between the sinkage and the contact zone. The tread elements proceed to drape over the larger asperities and to make contact with the lesser asperities.

3. Zone C –contact zone: This is the region where, for the most part, the tread elements have made contact with the road surface. Depending on vehicle velocity it occupies the rear part of the "contact" area. Almost all of the skid resistance is developed in this region.

These discontinuous interpretation of the three areas is not satisfactory for simulation or control purposes, because this requires a significant amount of characterizations and experimental measurements. In the next section we will propose a more sophisticated interpretation of the contact patch dynamics based on fluid mechanics to solve this problem.

3.3.2 Contact surface variation models

A preliminary version of this technique was presented in Moore (1964); further developments are given in Rohde (1975). This technique is very promising but has to be simplified for use in actual tire models. We first present some basic concepts from the literature and then study one example.

The main idea in Moore (1964) is to identify the dynamics of the sinkage of the tire when a thin film of water is present at the tire/road interface. The fluid at the interface is modeled as viscous, and the sinkage dynamics of the tire can be determined using for example the Navier-Stokes equations. At the time these studies were performed, computers were not sufficiently powerful, thus simple analytic solutions were developed. A numerical solution was also derived in Rohde (1975) using some simplifications.

The effective tire/road contact surface is a function of the time taken by the tire to achieve contact with the ground. As a consequence, all the parameter calculations are based on the water clearance time or time of sinkage. This time will vary for different wheel speeds, tread stiffness, ground pattern characteristics, etc.

Definition 3.1 *The sinkage time of the tire, Δt_2, is defined as the time for the water level to decrease from its initial height h_0 (h_0 is the initial height of water in the squeeze film area) to a final height h_{min}, where h_{min} is small enough so that we can consider that the tire and road surfaces are in contact.*

The time for a portion of the tire to cross the contact patch is given by $\Delta t_1 = \frac{L}{r\omega}$. If $\Delta t_1 > \Delta t_2$, the water level is not sufficient to completely prevent dry contact and the portion of the tire in dry contact has length

$$L^{water} = r\omega\left(\Delta t_1 - \Delta t_2\right) = Y_R L, \tag{3.13}$$

with Y_R being the fraction of the tire that is in real contact with the ground.

A simple method for solving this problem uses the analogy between the behavior of the tire in the sinkage zone, or squeeze film area, and the sinkage of a flat plate over a randomly rough surface area. Considering the sinkage of a flat plate over a rough surface, there is a bulk flow of escaping fluid between the plate and the asperity tips, and an open channel flow between asperities (called channelization). As the plate approaches the peaks of the asperities, there is virtually no bulk flow, and the channel flow becomes closed because the plate provides an upper boundary in this position.

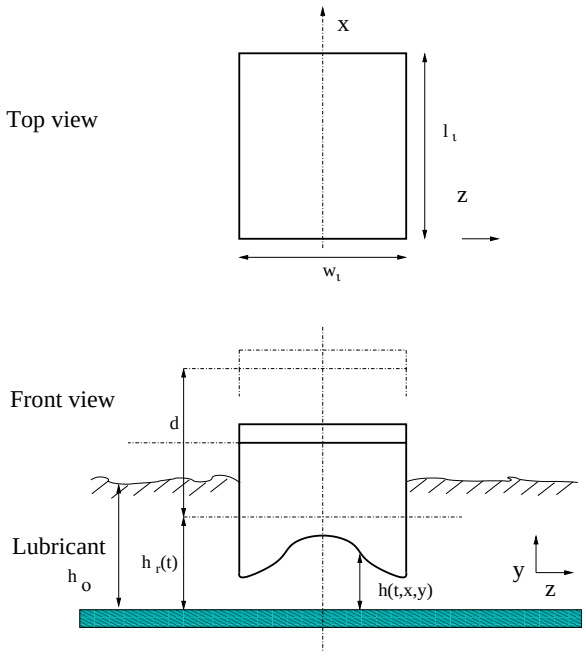

Figure 3.6: Film of water between a tread block and the ground, with h_0 being the water film thickness, d the tread element thickness, $h_r(t)$ the mean position of the tread element (assuming the tread is rigid) and $h(t, x, y)$ the position of the tread element (assuming that the tread is flexible)

This approach gives a good intuitive understanding of the problem (see Moore (1964)), but it is still very crude and we are currently looking for a better model. It appears that describing each tread element individually using viscous flow theory may provide such a model. Two solutions are important in the analysis of viscous flow at the interface:

1. Time varying solution: The Navier-Stokes equation for the flow is a partial differential equation. Identifying the time dynamics of the water level under the tire is difficult, since many parameters such as the tire tread stiffness, speed, etc. affect these dynamics. Several approximations are necessary to obtain an analytical solution to the problem. In this section, we will assume that the tire tread elements are rigid. Then, the Reynolds equation becomes a simple time-varying equation. The solution of this equation is important to evaluate whether water is removed quickly enough from the contact patch, in order to achieve dry friction.

2. Stationary solution: Finding a time-varying solution to the problem is not useful if one wishes to apply this theory to an actual tire model, since we want to determine the time for a tread element to contact with the ground and relate this quantity to the effective contact surface. Thus, as an alternative we will tune a static model with respect to the road conditions.

To derive a stationary solution for a circular tread element shown in top of Fig. 3.6, we will study the following governing equation for the descent of the tread element through a thin film of water:

$$\frac{1}{\wp}\frac{\partial}{\partial \wp}(\hbar^3 R\frac{\partial \wp}{\partial \wp}) = \frac{1}{\pi}\frac{d\hbar}{dt}\,, \tag{3.14}$$

where $\mathbb{p} = \frac{\rho}{\rho_0}$ is a normalized radius, ρ is the radial coordinate, ρ_0 is the tread radius, $\mathbb{h} = \frac{h_r}{h_0}$ is the normalized water height with h_0 is the initial height of water in the squeeze film area (for simplicity we take $h_0 = h_\infty/100$), $\mathbb{p} = \frac{p}{P_{ref}}$ is the normalized pressure with p is the tread pressure and $P_{ref} = \frac{12\nu v_{ref}\rho_0^2}{h_0^3}$, v_{ref} is a reference velocity and ν is the fluid viscosity.

The Reynolds Eq. (3.14) written in dimensionless form is valid only for a thin film of water ($h_0 < 0.2mm$). However if we assume that downward water inertia is removed in the hydrodynamic region of the upward thrust, this part of model describes only the thin squeezed film of water $h_r(t)$ remaining at the tire/road interface.

The effect of slip has been neglected in this equation, but can be added if necessary. However, in most cases, it turns out to be negligible. Since we are interested in the load $W(t)$ that the fluid supports at each instant of time, with $W(T) = 2\pi \int_0^1 \mathbb{p}(t,r)\mathbb{p}d\mathbb{p}$, we may integrate Eq. (3.14) to get

$$W(t) = -\frac{1}{2}\frac{d\mathbb{h}}{dt}\int_0^1 \frac{\mathbb{p}^3 d\mathbb{p}}{\mathbb{h}^3}\,. \tag{3.15}$$

Considering $\mathbb{h}$ as a constant at each instant of time, Eq. (3.15) then reduces to

$$W(t) = -\frac{1}{8}\frac{d\mathbb{h}}{dt}\frac{1}{\mathbb{h}^3}\,. \tag{3.16}$$

This equation can be solved for a simple time varying function $\mathbb{h}(T)$ with $T = \frac{tv_{ref}}{h_0}$ as the normalized time to obtain

$$\mathbb{h}(T) = \frac{1}{\sqrt{1 + I(T)}}, \tag{3.17}$$

with $I(T) = A\int_0^T W(\tau)d\tau$ and $A = 16$. Notice that the constant A in this expression will be different for different tread element geometries (for example. $A = 18.1$ for a square element instead of 16 for a round element). Thus, the above results are valid for other geometries.

We have described the descending dynamics of the tread in the fluid (in dimensionless form). Suppose that there is contact for $\mathbb{h} < \mathbb{h}_{min}$, where $\mathbb{h}_{min}$ is a given normalized limit spacing between the tire and the road ($\mathbb{h}_{min} = \frac{h_{min}}{h_0}$ and h_{min} is the minimum spacing between tire and road). Then, we can determine the setting time from the solution given in Eq. (3.17). Supposing that the pressure distribution is uniform and constant, we obtain this result in a non-normalized form

$$\Delta t_2 = \frac{12\nu\rho_0^2}{A\pi p}\left[\frac{1}{h_{min}^2} - \frac{1}{h_0^2}\right]. \tag{3.18}$$

Using this expression and definition 3.1, we can find Y_R in Eq. (3.13), the fraction of the tire in contact with the road.

Using the same method, it is possible to include the effect of the ground surface. This task is however more difficult and it is helpful to consider the work developed in Rohde (1975). A similar equation to (3.14) can be written if the ground texture is isotropic and a solution similar to Eq. (3.18) is obtained. In this case the setting time Δt_2 is a function of amplitude ϵ of the road texture. The texture will modify the mathematical expression of Δt_2. For a triangular road texture,

$$\Delta t_2 = \frac{12\nu\rho_0^2}{A\pi p}\left[\frac{1}{h_{min}^2 - \epsilon^2} - \frac{1}{h_0^2 - \epsilon^2}\right]. \tag{3.19}$$

Fig. 3.7 shows the setting time as a function of the water level h_0 for three different textures. We observe that the initial water level in the transition zone h_0 does not affect greatly the setting time. An interesting result is that the effective fraction of the tire in contact with the ground (Y_R) is a function of both the texture amplitude ϵ, and the angular wheel velocity w. In other words, for a given level of water on the road h_∞ and a fixed travel velocity v, the hydroplaning limit (or the adhesion characteristic) will vary only as a function of the road surface properties (texture and density) and the wheel acceleration input. Notice that in this example we have neglected the tread deformations, which could interfere with this process.

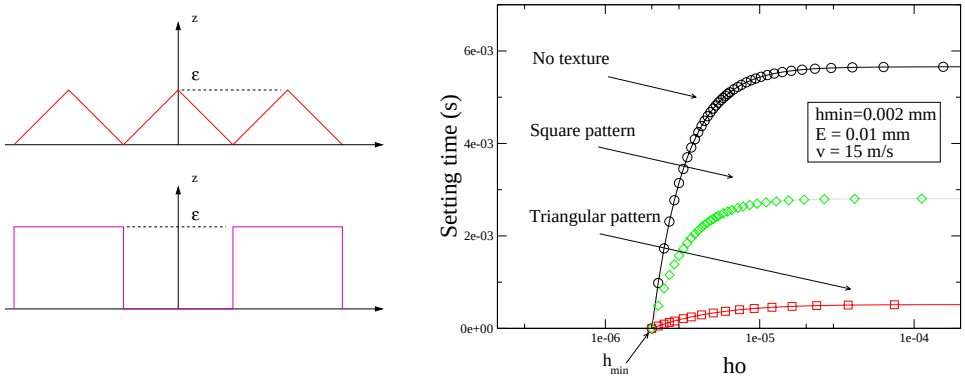

Figure 3.7: Effect of the pattern design on the setting time. For example, the setting time is smaller for a triangular pattern than for a squared pattern for the same texture amplitude. On the other hand no texture at all implies a larger setting time.

Using this result, we can now describe the tire behavior in wet road conditions as a function of the external condition (h_∞), the internal state (ω, v and F_z) and the road properties (ϵ, ρ_{tx}). Keeping track of the road texture properties becomes an important issue in tire/road friction modeling and estimation under wet road conditions. The following conclusions can be obtained preliminarily from the contact interface model that has been discussed.

1. In the case of a uniform tire pressure distribution, the normal force depends on the ratios Y_R and Y_F defined in previous sections (see Eqs. (3.11) and (3.13)):

$$F^{water} = \int_{-L/2}^{L/2} P w d\xi - \int_0^L P^{water} w d\xi = (Y_R - Y_F) F_z = Y_L F_z \tag{3.20}$$

2. The contact patch length has an expression which depends on the given ratio Y_R as well:

$$L^{water} = Y_R L \tag{3.21}$$

3.3.3 Three dimensional friction tire model under wet road conditions

We can modify the lumped LuGre dynamic friction model (Yi et al., 2002) for a tire/road friction model under wet road conditions using variation parameters Y_R and Y_L as

$$\begin{cases} \dot{z} = v_r - Y_R \frac{\sigma_0 |v_r|}{h(v_r)} z \\ F = Y_L (Y_R \sigma_0 z + \sigma_1 \dot{z} + \sigma_2 v_r) F_z \, . \end{cases} \tag{3.22}$$

For a pseudo-static case, we can use the three dimensional tire model developed in section 3.2 and discuss the consequences of previous results. We include the road condition given by Eqs. (3.20) and (3.21) in the model. The extended pseudo-static model in traction case is given by the following expression:

$$\frac{F_x}{F_z} = -Y_L\gamma_x(v_{sx})\,\mathrm{sign}(v_{sx})g_x(v_{sx})\left[1+\frac{h_x(v_{sx})}{Y_RL\sigma_{0_x}\lambda_{s_t}}(e^{-\frac{\sigma_{0_x}Y_RL\lambda_{s_t}}{h_x(v_{sx})}}-1)\right]+ Y_L(\sigma_{1_x}+\sigma_{2_x})v_{sx} \tag{3.23a}$$

$$\frac{F_y}{F_z} = -Y_L\gamma_y(v_{sy})\,\mathrm{sign}(v_{sy})h_y(v_{sy})\left[1+\frac{h_y(v_{sy})}{Y_RL\sigma_{0_y}\lambda_{\alpha_t}}(e^{-\frac{\sigma_{0_y}Y_RL\lambda_{\alpha_t}}{h_y(v_{sy})}}-1)\right]+ Y_L(\sigma_{1_y}+\sigma_{2_y})v_{sy} \tag{3.23b}$$

$$\frac{M_z}{F_z} = -Y_L\frac{\gamma_y(v_{sy})\,\mathrm{sign}(v_{sy})g_y^2(v_{sy})}{2\sigma_{0_y}^2\lambda_{\alpha_t}}\left[\left(e^{-\frac{\sigma_{0_y}Y_RL\lambda_{\alpha_t}}{h_y(v_{sy})}}-1\right)+ \frac{2h_y(v_{sy})}{Y_RL\sigma_{0_y}\lambda_{\alpha_t}}\left(e^{-\frac{\sigma_{0_y}Y_RL\lambda_{\alpha_t}}{h_y(v_{sy})}}-1\right)\right], \tag{3.23c}$$

where γ_i, σ_{i_j}, h_j, $i=0,1,2$, $j=x,y$ are the same as those in Eq. (3.8). For the braking case a similar formula can be derived with $\lambda_{s_t}=\frac{\lambda_{s_b}}{1-\lambda_{s_b}}$ and $\lambda_{\alpha_t}=\frac{\lambda_{\alpha_b}}{1-\lambda_{s_b}}$.

3.3.4 Numerical example

The results of a numerical simulation are illustrated in Figs. 3.8 and 3.9 for a typical tire referenced as 165-$65\mathrm{R}14$ under wet road conditions. The model was first tuned to fit the classical "magic formula" on a dry surface, and then it was simulated for different water films and various texture amplitudes. Fig. 3.8 illustrates the hydro-dynamic properties of the tire under wet road conditions. As predicted, increasing the thickness of the water on the road h_∞ for a given travel velocity v dramatically reduces the resulting friction. Furthermore, Fig. 3.9 shows the effect of varying the texture amplitude ϵ on the friction characteristics. In this case, the water layer h_∞ is given and the road pattern is specified as triangular. As ϵ is varying the setting time is slightly affected. We observe that friction increases as texture amplitude increases.

3.4 Conclusions

In this chapter, we first discussed a general framework to extend a physical tire/road friction model. Different physical variations were considered in the extension. Particularly, we first extended and derived a three dimensional dynamic tire/road friction model, based on previous work which had only considered longitudinal motions. Both distributed and lumped friction models were discussed. The lumped model can be used to identify the tire/road conditions and can be applied to vehicle control. A numerical example was presented to calibrate the model parameters and validate the model with respect to the widely used "magic formula". From the analysis and numerical results obtained, we found that the proposed friction model can capture the tire/road friction characteristics and can easily be used for friction estimation and control purposes. In the latter part of this chapter, we also considered a dynamic friction model under wet road conditions, based on the developed

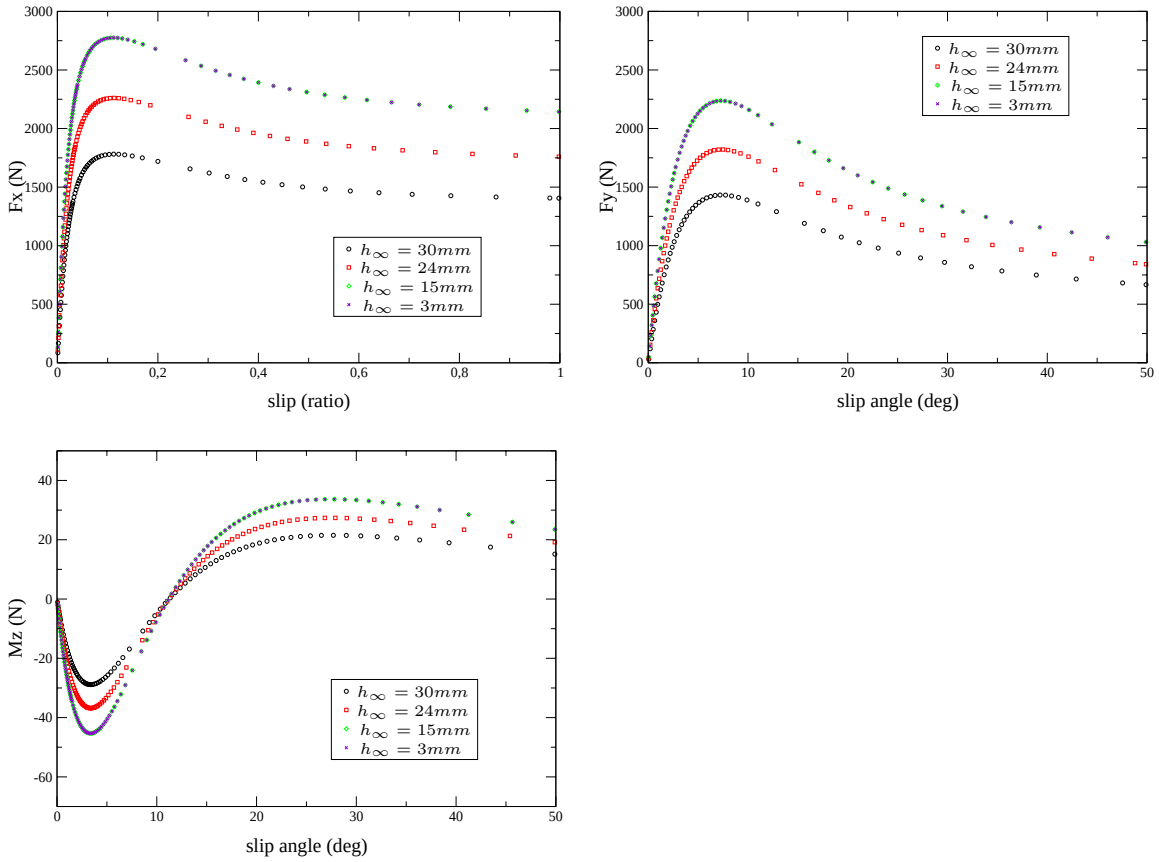

Figure 3.8: Effect of water depth h_∞ on a stationary tire model ($v = 25m/s$ and triangular texture of amplitude $\epsilon = 0.06mm$)

three dimensional dynamic tire model. In particular, both the hydro-dynamic and lubrication effects of the contact zone have been discussed. Different road textures and densities can be introduced in dynamic friction tire models using relatively simple methods. Furthermore, a technique to decouple the effects of the road pavement from those of the tire under wet conditions has been proposed, and could lead to an important breakthrough for embedded road or vehicle diagnostic tools.

3.5 Future Research Directions

We have discussed many aspects of tire/road friction models, estimation and emergency braking control in this project. Several aspects in this area can be extended, and are mentioned here as future work:

3.5.1 Model enhancements

In MOU 373 (Yi et al., 2002), we discussed the applications of the LuGre dynamic friction model to the estimation of the tire/road friction characteristics. We made a few assumptions and some of these assumptions are not entirely realistic. For example, we assumed a uniformly distributed

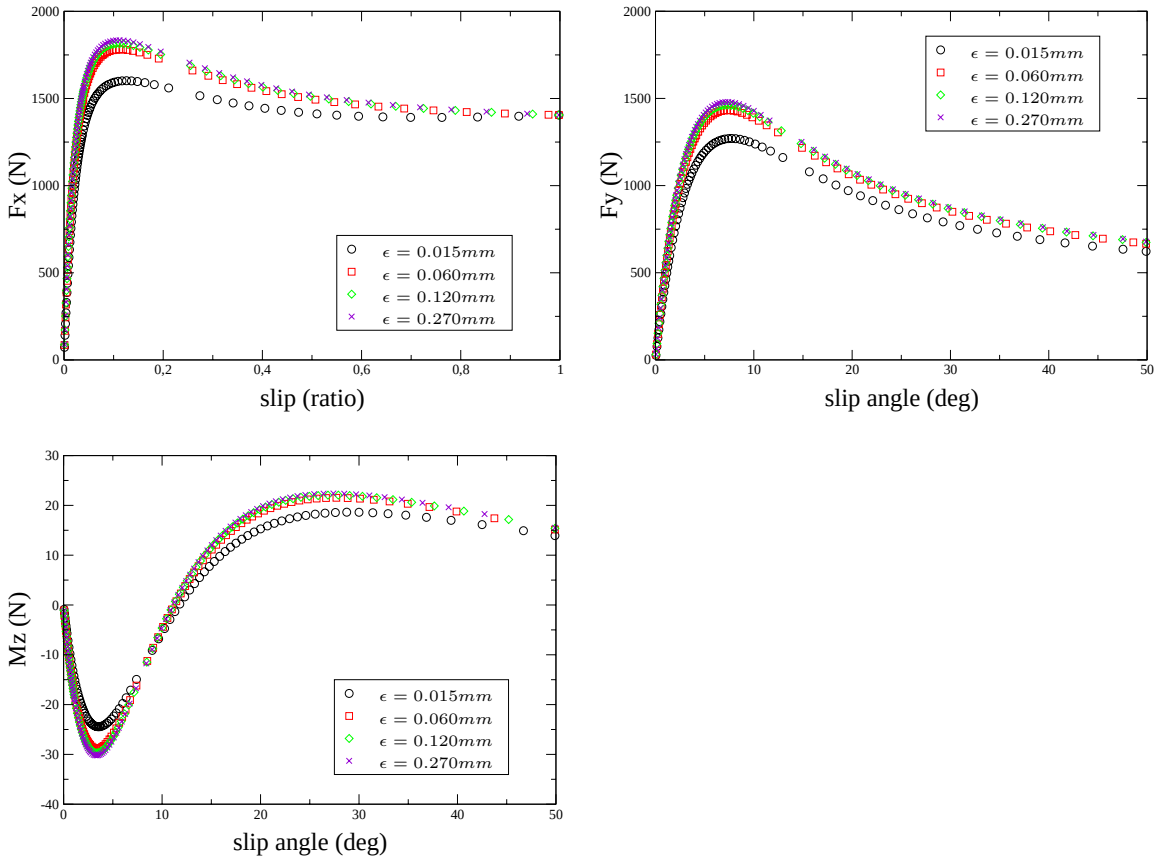

Figure 3.9: Effect of road texture amplitude E on a stationary tire model (texture: triangular motif, $v = 25m/s$ and $h_\infty = 30mm$)

pressure on the tire/road contact patch and no coupling effect between the lateral and longitudinal friction forces. Enhancements to the tire/road friction model using the LuGre dynamic friction model will require relaxation of these two assumptions. In Deur (2001), a modified LuGre dynamic model has been studied for different normal force distributions. The modified lumped LuGre model is given in Yi et al. (2002). Introducing the extra term κ into the friction model does not dramatically change the emergency braking controller design. We can easily modify the controller design since the wheel angular velocity ω is measurable. More recently, Deur et al. (2001) extended the modified LuGre friction model to study combined longitudinal and lateral vehicle motions. A simple coupling mechanism was also developed in Deur et al. (2001).

In order to understand the tire/road interactions completely, extension of the modified LuGre model in Chapter 5 in Yi et al. (2002) to various physical conditions should be investigated. In MOU 373 (Yi et al., 2002), we only demonstrated the case of the tire model under wet road conditions. The effects of other physical variations, such as changes in tire pressure and temperature, require further study. In MOU 373, we also used a three-dimensional model of the tire/road friction in which longitudinal and lateral effects are decoupled. Further improvements to the model should also include an investigation of the interaction of longitudinal and lateral motions. Once we understand the friction models under various conditions, we can explore more estimation and control issues.

3.5.2 Experimental validations

The proposed tire/road friction models presented in this project were validated using numerical methods. Experimental validations using a real vehicle setup are necessary and worthwhile at this stage.

To test the pseudo-static tire/road friction scheme discussed in MOU 312 and the dynamic friction scheme in Part I of this project report, we can use the red Lincoln Town Car at Richmond Field Station (RFS) at University of California at Berkeley campus. The hardware setup has been developed under previous PATH research projects (Hedrick and Uchanski, 2001; Uchanski, 2001), which makes real-time implementation and testing feasible. Table 3.2 shows the availability of measurements on the red Lincoln Town Car. Specifically we need access to the measurements of wheel angular velocity, vehicle velocity, acceleration, braking pressure and braking torque. All of these variables, except vehicle velocity, can be obtained from sensors already installed on the vehicle. Vehicle velocity can be obtained using an additional fifth wheel or with the global positioning systems (GPS) facilities at the RFS. Experiments can be performed in two steps: the first consisting of open-loop tests where the friction estimation scheme is run for safety purposes, and the second step introducing closed-loop braking control.

Table 3.2: Sensors and Measurements on the red Lincoln Town Car at the RFS

Sensors	**Specifications of Measurements**
Wheel speed sensor	Measuring angular velocity for each wheel. *Fairly accurate*
Brake pressure sensors	Measuring brake pressure for each wheel and for master cylinder. *Accurate*.
Accelerometer	Measuring the longitudinal acceleration. *Pretty noisy*.
Brake torque sensor	Measuring only the *front left* wheel braking pressure. *Accurate*
Engine pressure sensor	Measuring the engine manifold pressure. *Accurate*
Engine temperature sensor	Measuring the engine manifold temperature. *Accurate*
Engine speed sensor	Measuring the engine speed. *Accurate*
Transmission speed sensor	Measuring the transmission carrier speed. *Accurate*

Experimental validations of the extension to the dynamic friction models discussed in MOU 373 (Yi et al., 2002) are much more complicated since it requires more measurements, such as tire internal pressure and temperature, etc. Recently, Pohl et al. (1999) has introduced the concept of the “intelligent tire”, in which the tire is equipped with sensor systems to monitor thermal and mechanical parameters during motions. In Pohl et al. (1999) and Yilmazoglu et al. (2001), passive surface acoustic wave (SAW) sensors and magnetic field sensors have been used to measure the tire tread deformation, respectively. In Reindl et al. (2001), SAW-based radio sensor systems have been proposed to measure the physical quantities such as temperature, pressure, torque, acceleration, etc. Recent advancements such as these will enable us to use newly-developed telematic sensor technology to validate and develop the new tire/road friction models. Application of new sensors to enhance the tire/road friction model, thus improving vehicle stability, is a promising research direction.

3.5.3 Cooperative estimations

In this project, we discussed different approaches for tire/road friction estimation schemes. These schemes do not depend on whether the vehicle is manual or automated. However, an AHS, even though the friction estimation schemes converge very quickly compared with other approaches, we have not made use of an important advantage of the fact that there is a considerable amount of communication between the roadside and the vehicles. Each vehicle in an AHS can use the tire/road friction estimation scheme developed in this project to calculate its friction coefficient, and can then broadcast this information to the roadside system, along with other information such as vehicle position, velocity, etc. The roadside computer systems can process this data and feed back spatial friction characteristics for the highway. This information can then be used to enhance vehicle and platoon safety and performance. In other words, each vehicle on the highway is potentially a road-condition "sensor" which can relay its experience to the roadside through the communication infrastructure in order to form a composite snapshot of the highway's friction characteristics.

In future research, we can use a model-based cooperative friction estimation scheme for the AHS. Specifically we can use the friction estimation scheme for individual vehicles and a method can be designed and investigated for decoupling the friction information into a spatial function along the highway and a set of vehicle-dependent functions. In Hedrick et al. (2001), a similar approach has been discussed. However, the proposed work is a different approach and will complement the work of Hedrick et al. (2001) [6].

In this Chapter we discussed how different tire and road conditions affect the friction characteristics for each vehicle, and a hierarchical physical friction model was presented. If we reconsider the varying conditions in the vehicle and road domains, we can exploit a different approach to friction estimation by using the friction information of many vehicles on the same piece of highway. Fig. 3.10 illustrates the hierarchical structure for a cooperative friction estimation scheme. We consider N vehicles with different characteristics, such as weight, tire types and flatness, passing through one position on the highway. Each vehicle measures or estimates the friction coefficient at this position and transfers this information to the roadside system. Thus we can collect the friction coefficient data, $\mu = \{\mu_1, \mu_2, \cdots, \mu_N\}$. Moreover, the varying tire and road conditions can be either measured or observed; for example, each car knows how flat its tires are, and road pavement can also be evaluated and classified a priori. The roadside systems can also access this information. In Fig. 3.10 we use shadowed nodes to stand for measurable (or observable) variables and white nodes for unknown variables. As we can see in the picture, as N vehicles pass through the same place on the highway, we can visualize that the friction characteristics are statistically determined by two decoupled functions: vehicle-dependent and road-dependent functions. The vehicle-dependent function is different for each vehicle and changes with vehicle load, tire type and flatness of tires, etc. However, since all vehicles pass through the same place on the highway, the road-dependent functions are the same for each vehicle. In Fig. 3.10 we use a dashed box with the number N to indicate the variables that change for different vehicles. We do not know what the analytical form for vehicle-dependent and road-dependent functions are due to the complexity of tire/road friction and vehicle types. However, we do know how the varying tire/road conditions affect the friction

[6] The differences can be found in following respects: (1). The cooperative friction estimation scheme in Hedrick et al. (2001) assumes that a linear relationship between friction coefficient μ with slip λ, while in our case we drop such assumption; (2) only two parameters were used to capture the μ-λ relationship in Hedrick et al. (2001). We consider a more general μ-λ form.

characteristics, as discussed in this Chapter. For example, from preliminary studies, we know that the water level on the road surface can be modeled by inserting Y_R and Y_L into the dynamic friction model given by Eq. (3.22) in this Chapter. This functional relationship can be used to estimate the road-dependent function. Once the road-dependent function at one place has been estimated, it will be used to predict the tire/road friction for all the other vehicles in the platoon that will pass that point later, which will lead to enhancement of the AHS safety and performance. Some forms of statistical learning theory can be used preliminarily to identify the road-dependent friction function when N is large, which is the case in AHS, for example, the hierarchical mixture of experts (HME) discussed by Jordan and Jacobs (1994). As a consequence, the communication capability used for cooperative friction estimation has been studied and modified.

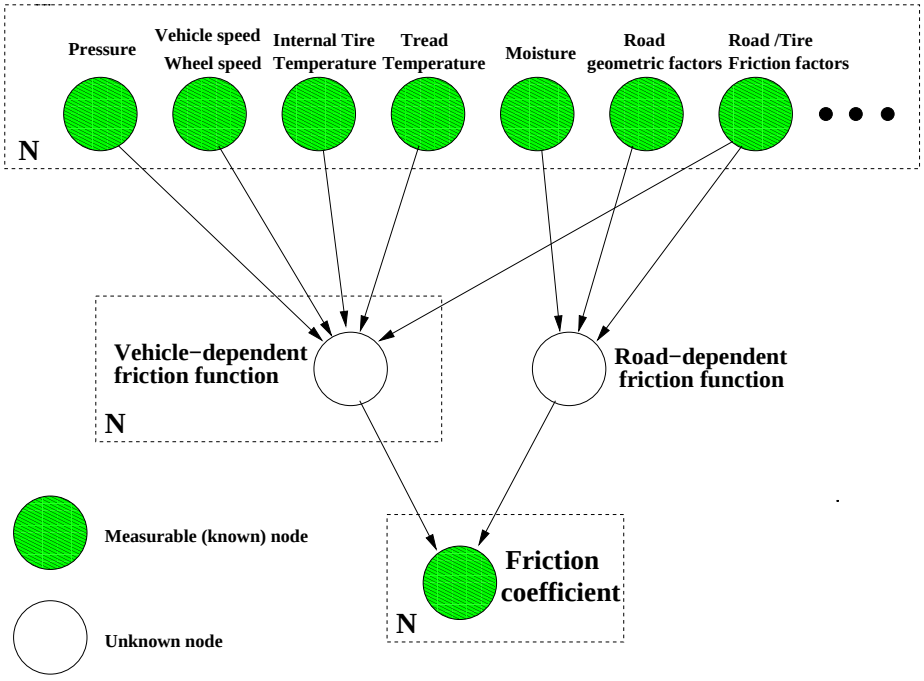

Figure 3.10: A hierarchical structure of cooperative friction estimation for N vehicles passing through the same place on the highway (arrow stands for "affects").

Bibliography

Agogino, A., Goebel, K. and Alag, S.: 1997, Intelligent Sensor Validation and Sensor Fusion for Vehicle Guidance Using Probabilistic and Fuzzy Methods, *PATH Research Report UCB-ITS-PRR-97-31*, Institute of Transportation Studies, University of California at Berkeley.

Bakker, E., Nyborg, L. and Pacejka, H. B.: 1987, Tyre Modeling for Use in Vehicle Dynamics Studies, *SAE Transactions* (870421), 190–204.

Browne, A. and Whicker, D.: 1977, Design of tire tread elements for optimum thin film wet traction, *SAE Transactions* (770278).

Burckhardt, M.: 1987, *ABS und ASR, Sicherheitsrelevantes, Radschlupf-Regel System, Lecture Scriptum*, University of Braunschweig, Germany.

Canudas de Wit, C. and Tsiotras, P.: 1999, Dynamic Tire Friction Models for Vehicle Traction Control, *The* 38*th IEEE Conference of Decision and Control*, Phoenix, AZ.

Carbaugh, J., Alvarez, L., Chen, P. Y. and Horowitz, R.: 1997, SmartPATH Regulation Layer Implementation: A User's Guide, *PATH Research Reports UCB-ITS-PRR-97-48*, Institute of Transportation Studies, University of California at Berkeley.

Chen, P. Y., Alvarez, L. and Horowitz, R.: 1997, Trajectory Design and Implementation of Longitudinal Maneuvers on Automated and Transition Lanes, *PATH Research Reports UCB-ITS-PRR-97-49*, Institute of Transportation Studies, University of California at Berkeley.

Chung, R. K. D. W., Malladi, D., Chen, R., Speyer, J. L. and Mingori, D.: 1996, Fault Detection and Identification with Application to Advanced Vehicle Control Systems: Final Report, *PATH Research Report UCB-ITS-PRR-96-25*, Institute of Transportation Studies, University of California at Berkeley.

Chung, R. K. D. W., Malladi, D., Chen, R., Speyer, J. L. and Mingori, D.: 1997, Fault Detection and Identification with Application to Advanced Vehicle Control Systems, *PATH Research Report UCB-ITS-PRR-97-51*, Institute of Transportation Studies, University of California at Berkeley.

Deur, J.: 2001, Modeling and Analysis of Longitudinal Tire Dynamics Based on the LuGre Friction Model, *The Proceedings of the IFAC Conference on Advances in Automotive Control*, Kalsruhe, Germany, pp. 101–106.

Deur, J., Asgan, J. and Hrovat, D.: 2001, A Dynamic Tire Friction Model for Combined Longitudinal and Lateral Motion, *Proceedings of 2001 ASME International Mechanical Engineering Congress and Exposition*, New York, NY.

Garg, V.: 1995, *Fault Detection in Nonlinear Systems*, PhD dissertation, Department of Mechanical Engineering, University of California at Berkeley.

Gim, G. and Nikravesh, P.: 1990, An analytical model of pneumatic tyres for vehicle dynamic simulations. Part I: Pure slips, *International Journal of Vehicle Design* **11**(6), 589–618.

Godbole, D., Lygeros, J., Singh, E., Deshpande, A. and Lindsey, A.: 2000, Communication Protocols for a Fault-Tolerant Automated Highway System, *IEEE Transactions on Control Systems Technology* **8**(5), 787–800.

Hedrick, J. and Uchanski, M.: 2001, Brake System Modeling and Control, *PATH Research Report UCB-ITS-PRR-2001-25*, Institute of Transportation Studies, University of California at Berkeley.

Hedrick, J., Uchanski, M. and Xu, Q.: 2001, Enhanced AHS Safety Through the Integration of Vehicle Control and Communication, *PATH Research Report UCB-ITS-PRR-2001-28*, Institute of Transportation Studies, University of California at Berkeley.

Horne, W. and Buhlmann, F.: 1983, A method for rating the skid resistance of micro/macrotexture characteristics of wet pavements, *Frictional Interaction of Tire and Pavement, American Society for Testing and Materials*.

Jordan, M. I. and Jacobs, R.: 1994, Hierarchical Mixtures of Experts and the EM Algorithm, *Neural Computation* **6**(2), 181–214.

Lygeros, J., Godbole, D. and Broucke, M.: 2000, A Fault Tolerant Control Architecture for Automated Highway Systems, *IEEE Transactions on Control Systems Technology* **8**(2), 205–219.

Moore, D.: 1964, Drainage criteria for runway surface roughness, *Royal Aeronautical Society*.

Patwardhan, S.: 1994, *Fault Detection and Tolerant Control for Lateral Guidance of Vehicles in Automated Highways*, PhD dissertation, Department of Mechanical Engineering, University of California, Berkeley, California.

Pohl, A., Steindl, R. and Reindl, L.: 1999, The "Intelligent Tire" Utilizing Passive SAW Sensors – Measurement of Tire Friction, *IEEE Transactions on Instrumentation and Measurement* **48**(6), 1041–1046.

Pottinger, M. and Yager, T.: 1985, *The Tire Pavement Interface*, ASTM Publication. ASTM Publication Code Number 04-929000-27.

Rajamani, R., Hedrick, K. and Howell, A.: 1997, A Completed Fault Diagnostic System for Longitudinal Control for Automated Vehicles, *Proceedings of ASME Dynamic Systems and Control Division, ASME International Mechanical Engineering Congress and Exposition*, Dullas, TX.

Rajamani, R., Howell, A., Chen, C., Hedrick, J. and Tomizuka, M.: 2001, A Complete Fault Diagnostic System for the Longitudinal Control of Automated Vehicles, *IEEE Transactions on Control Systems Technology* **9**(4), 553–564.

Reindl, L., Pohl, A., Scholl, G. and Weigel, R.: 2001, SAW-Based Radio Sensor Systems, *IEEE Sensor Journal* **1**(1), 69–78.

Rohde, S.: 1975, On the effect of pavement microtexture on thin film traction, *International Journal of Mechanical Science* **18**(1), 95–101.

Rohde, S.: 1977, On the combined effects of tread element flexibility and pavement microtexture on thin wet traction, *SAE Transactions* (770277).

Sorine, M. and Szymanski, J.: 2000, A New All-Vehicle-Speed Dynamic Tire Model, *Proceedings of IFAC Symposium on Control in Transportation Systems*, Braunschweig, Germany.

Staff: 1998, Avcs vehicle-follower longitudinal control technologies: Final report, *Technical report*, California PATH. Research Agreement 65V313-001.

Suryanarayanan, S. and Tomizuka, M.: 2001, Lateral control of automated vehicles: On degraded mode control problems, *Proc. of the* 41^{st} *International Mechanical Engineering Congress and Exposition, New York*, pp. 899–904.

Uchanski, M.: 2001, *Road Friction Estimation for Automobiles Using Digital Signal Processing Methods*, PhD dissertation, Department of Mechanical Engineering, University of California at Berkeley.

Varaiya, P.: 1993, Smart Cars on Smart Roads: Problems of Control, *IEEE Transactions on Automatic Control* **38**(2), 195–207.

Yi, J., Howell, A., Horowitz, R., Hedrick, K. and Alvarez, L.: 2001, Fault Detection and Handling for Longitudinal Control of Automated Highway Systems (AHS), *PATH Research Report UCB-ITS-PRR-2001-21*, Institute of Transportation Studies, University of California at Berkeley.

Yi, J., Suryanarayanan, S., Howell, A., Horowitz, R., Tomizuka, M., Hedrick, K. and Alvarez, L.: 2002, Development and implementation of a vehicle-centered fault diagnostic and management system for the extended path-ahs architecture: Part i. Submitted as California PATH Technical Report.

Yilmazoglu, O., Brandt, M., Sigmund, J., Genc, E. and Hartnagel, H.: 2001, Integrated InAs/GaSb 3D magnetic field sensors for "the intelligent tire", *Sensors and Actuators* **A**(94), 59–63.